CrystEngComm

Accepted Manuscript

ROYAL SOCIETY OF CHEMISTRY

www.rsc.org/crystengcomm

Flux-Mediated Crystal Growth of Metal Oxides: Synthetic Tunability of Particle Morphologies, Sizes, and Surface Features for Photocatalysis Research

Jonathan Boltersdorf, Nacole King, and Paul A. Maggard*
Department of Chemistry, North Carolina State University, Raleigh, NC 27695-8204
E-mail of corresponding author: pamaggar@ncsu.edu

I. ABSTRACT

Molten-salt reactions can be used to prepare single-crystal metal-oxide particles with morphologies and sizes that can be varied from the nanoscale to the microscale, subsequently enabling a growing number of novel investigations into their photocatalytic activities. Crystal growth using flux-mediated methods facilitates finer synthetic manipulation over particle characteristics. The synthetic flexibility that flux synthesis affords for the growth of metal-oxides has led to the stabilization of phases limited stability, the discovery of new compositions, and access to alternate crystal morphologies and sizes that exhibit significant changes in photocatalytic activities at their surfaces, such as for the reduction of water to hydrogen in aqueous solutions. This approach has significantly impacted the current understanding of the optical and photocatalytic properties of metal-oxides, such as the dependence of band gap energies on the structure and chemical composition (i.e., obtained from flux-mediated ion-exchange reactions). Thus, flux preparations of metal-oxide photocatalysts assist in the growth and optimization of their particles in order to understand and tune the photocatalytic reaction rates at their surfaces.

Keywords: Flux synthesis, molten-salt, crystal growth, ion-exchange, photocatalysis, solar energy conversion

II. INTRODUCTION

Current synthetic challenges for the crystal growth of complex oxides can be addressed by utilizing flux synthetic methods, which has made a significant impact in research involving solar energy conversion. The flux synthetic method is a modification of the high-temperature solid-state ceramic method that involves the addition of a molten-salt solvent to facilitate crystal growth with improved phase-purity and particle homogeneity.[1–6] The flux synthetic route requires the use of an inorganic salt heated above its melting temperature in order to dissolve solid inorganic reactants and to serve as a solvent system for crystallization. Crystal growth in a molten flux can be described to occur in four steps: i) reactant dissolution; ii) reactant diffusion through the molten flux; iii) nucleation; and iv) subsequent crystal growth of the product from the nuclei.[1,3,7–11] The flux solvent approach facilitates the growth of crystals below the melting points of the constituent reactants and desired products, thereby allowing for lower reaction temperatures.[1,2]

The flux-mediated growth of single-crystals allows for the exploration of new compositions and structures in order to investigate their physical properties. Flux-mediated crystal growth can yield high-quality crystals suitable for single-crystal X-ray diffraction.[1–3,5,7] Many reports have demonstrated the remarkable effectiveness and utility in using flux synthesis.

For example, a recent review by zur Loye et al[7] provides an overview of high-temperature molten fluxes for crystal growth and materials' discovery of complex oxides. Flux-mediated crystal growth also affords the synthetic control over crystallite morphologies, sizes, and surface features.[7,12–22] In particular, the synthetic flexibility afforded by flux-mediated crystal growth methods has led to an increased interest in the exploration of new ternary and quaternary mixed-metal oxides for use in suspended particle photocatalysis for total water splitting. Studies focused on the modification of particle sizes, morphologies, and surface features as a function of flux conditions have been shown to yield significant enhancements in photocatalytic rates.[12,13,19–21,23–32]

This highlight is focused on the preparation of ternary and quaternary metal oxides using molten-salt flux synthesis methods and their use in suspended-particle photocatalysis research for the conversion of solar energy to chemical fuels. A comparison of conventional solid-state and flux synthetic methods will be described, together with the advantages and design strategies for the targeted preparation of crystalline metal-oxides using molten salts. Next, the role of the flux reaction conditions to control the particle morphologies and sizes will be related to their resulting properties at the surfaces. Finally, strategies for the discovery of new compositions and phases with limited stability will be discussed with relevance to solar energy conversion.

III. SOLID-STATE VERSUS FLUX METHODS

The most commonly utilized synthetic technique for crystal growth of complex oxides is the high temperature ceramic (or solid-state) method. The solid-state method typically involves combining stoichiometric proportions of solid inorganic reagents into a well-mixed fine powder in order to maximize the interfacial surface area. The well-ground mixtures are typically heated in a high-temperature furnace between 500 and 2000 °C in alumina or platinum crucibles. High temperatures and surface areas are necessary in order to increase the reaction rate and to shorten the ion diffusion paths. The rate of diffusion is often the limiting step owing to the fact that solid-state reactions only take place at the interface of the solid reactants in the absence of a solvent.[2,3,7–9,33] The mixtures can be pressed into a pellet to increase the direct contact of the crystallites. The solid-state method can require several cycles of grinding and reheating at high temperatures in order to yield a high-purity crystalline metal-oxide. Particle dimensions and morphologies are typically irregular, with limited synthetic control using solid-state methods.[3,7,9]

The flux synthetic method provides an approach for the nucleation and growth of a metal-oxide in a molten-salt solution through the dissolution of inorganic reagents and the resulting precipitation of the desired metal-oxide crystals.[1–4,7,8,34] Lower reaction temperatures in a flux solvent system result in highly crystalline and well-defined faceted surfaces.[2] Crystal growth at lower temperatures can allow phases to form without heating above a temperature at which the desired material would not be stable, or where an irreversible phase transition could occur.[3,7] Incongruently melting and highly non-stoichiometric mixtures are typically crystallized using a flux in order to avoid the formation of an undesired phase.[1–3,7,8] The enhancement of reaction kinetics and crystal growth in molten salts has been experimentally observed throughout the literature; however, little is known about the mechanisms and kinetic pathways in the solid-state or molten-salt fluxes.[7,35–37] Early stages of reaction kinetics in solid solutions are beginning to be investigated by in-situ powder X-ray diffraction experiments, which have shown enhanced reaction kinetics and crystal formation when using a molten flux in comparison to solid-state reactions. Reaction times as a result of using a molten flux have been reduced from 24-96 h down to as low as 15 min for the formation of mixed-metal oxides, such as $NaTi_2O_4$, $CuNb_3O_8$, and $RbCa_2Nb_3O_{10}$.[15,19,21,27,35,36,38]

The molten flux covers the surfaces of all reactant particles, preventing aggregation and sintering that are typically observed in solid-state reactions. The coating of all surfaces with the flux acts to increase the degree of homogeneity, to control the agglomeration level and anisometric particle growth, and to prepare well-defined uniform particle distributions. The presence of the molten flux promotes the formation of well-defined faceted particles with fewer grain boundaries, as typically observed in single-crystal growth from aqueous solutions.[1–3,5,7,8] Prolonged heating of the reactant mixtures in a flux enhances the material transport in the solution, and can increase the average particle size over time by Ostwald ripening.[2,3,7] Furthermore, adjusting the growth rates of metal-oxide surfaces can yield particles with cube, octahedron, or cuboctahedron morphologies, such as shown for $Pb_3Ta_4O_{13}$ in Figure 1 when the growth rates along the [100], [111], or intermediate growth are predominant for cubic systems, respectively.[1–3,7] Crystallographic anisotropy governs anisotropic crystal growth, while isotropic cubic crystal structures tend to form cube morphologies in molten salts. The greater the degree of structural anisotropy, the more likely the formation of 1D rods, 2D platelets, or more complex morphologies with differing exposed crystal facets.[34] The growth rates of the exposed crystal facets are highly dependent upon the choice of flux, degree of supersaturation of the flux solution, and the reaction conditions.[1–3,5,7,37,39,40]

It has been theorized that stable terminating crystal facets develop from equilibrium faces with the lowest free energy.[39] These facets typically exhibit lower Miller indices and have higher atomic packing densities. Preferential growth of crystal facets and anisotropic crystal morphologies may result, and are dependent upon the growth mechanism of the particle.[1–3,7,39] For example, flux synthesis of the photocatalysts $La_2Ti_2O_7$ and $Na_2Ta_4O_{11}$, both grown in a Na_2SO_4/K_2SO_4 molten flux, have shown preferential growth of {100} and $\{0001\}$, $\{10\bar{1}2\}$, and

$\{10\bar{1}4\}$ terminating crystallographic facets at their surfaces, respectively.[19,25] Layered perovskite structures favor preferred crystal growth of habit planes that typically facilitate the exposure of the $\{001\}$ system of planes at the flat platelet surfaces.[18,23–26,41] Distinct crystal facets for metal oxides have been commonly observed as a function of flux reaction conditions; however, investigations have not shown how to selectively express desired facets for complex oxides. The synthetic control over the exposed crystal faces is useful in probing reactions at the surfaces and identifying preferential anisotropic photocatalytic properties.

IV. FLEXIBILITY OF FLUX SYNTHESIS CONDITIONS

Appropriate selection of a flux in the synthesis of metal-oxide particles has been used to increase the particles' crystallinity and specific surface area, as well as yield more well-defined and faceted surface features.[12,13,16,17,19,23–25,42] Synthetic manipulation of the particles dimensions and their surface features is dependent on the choice of flux, the flux-to-reactant molar ratios, synthesis temperatures, heating/cooling times, and other conditions.[12,13,15,19,21,24,25,42] As shown in Table 1, flux solvents have been selected from an extensive array of metal oxides, hydroxides, halides, and oxosalts in order to yield a wide range of ternary or quaternary metal oxides. In practice, the flux and reaction conditions are typically chosen by a trial and error procedure, taking into account the solubilities of the reactants within the flux and the experimental trends from the literature. The necessary flux conditions are unique to each reaction system. However, an appropriate flux should have a relatively lower melting point compared to any of the reactants, low volatility, and should be able to be easily removed, such as by washing, in order to isolate the products.[7]

A. CHOICE OF FLUX SOLVENT

In order to solubilize inorganic reagents in a flux, the physical and chemical properties of the solute and solvent, such as the polarizability, ionic or covalent bonding, electronegativity, and common cations/anions, should be similarly matched. The solubilities of metal oxides in molten fluxes have been previously studied using thermodynamic and potentiometric determination methods.[43–52] The use of fluxes with the same cations as the desired metal-oxide typically yields phase-pure crystals as a result of the similar chemical bonding, coordination site preferences, electronegativity, and crystal radii. As a general guideline, the hard–soft acid–base (HSAB) theory can be used to predict solubility of inorganic reactants in molten-salt fluxes. Typically, metal cations are soluble in their corresponding metal halide fluxes; additionally, halide fluxes can exhibit mineralizing effects. Salt fluxes that can act as mineralizers include hydroxides (e.g., NaOH, KOH, LiOH), carbonates (e.g., Na_2CO_3), and halides (e.g., NaF, KF, NaCl, KCl).[3–5,7,53–55]

Oxosalt solvent systems, such as hydroxides, nitrates, carbonates, and sulfates, are suitable fluxes for solubilizing metal oxides owing to their acid-base chemistry. The solubility of metal oxides in oxosalts can be described by the concentration of oxygen anions in solution using the Lux–Flood (L–F) type acid–base equilibrium, in which the acid is defined as an O^{2-} acceptor, the base is defined as an O^{2-} donor, and the ‘‘neutral’’ species as OH^-. For example, under moderately basic conditions the precipitation of metal oxides (e.g., TiO_2) can occur in a molten oxosalt flux. However, with increasing basicity metal oxides can be dissolved into the flux to form metallate complexes (e.g., TiO_3^{2-}) that can further react with cations in solution to form mixed-metal oxides. In the case of a PbO flux with a TiO_2 precursor, the flux liberates O^{2-} anions in solution to dissolve TiO_2 into TiO_3^{2-} under basic conditions, which can then react with Pb^{2+} cations in solution to form $PbTiO_3$.[3–5,7,13,22,31,54–62] Molten fluxes that tend to form strongly oxidizing species or complex metallates in solution act to stabilize structures with higher oxidation states.

Molten-salt fluxes can also be used in binary combinations to form eutectic mixtures that are advantageous owing to their reduced melting points and lower viscosity, e.g., NaCl-KCl and Na_2SO_4-K_2SO_4. These two eutectic fluxes have been widely used in the literature for the crystal growth of metal oxides, such as listed in Table 1. For example, the melting points of NaCl and KCl are 801 °C and 770 °C, respectively, but the melting point of a 50% NaCl and 50% KCl eutectic mixture has a reduced melting temperature of 650 °C.[3,10] Available databases of thermodynamic phase diagrams can aid in selecting the appropriate molar ratio and melting point of a eutectic mixture. An excellent online resource is the FactSage FTsalt thermochemical software and database available through the École Polytechnique de Montréal.[63] Identifying the ideal flux solvent or eutectic flux system for a given reaction is typically accomplished using the general guidelines given by HSAB theory, Lux-Flood theory, and the desired reaction conditions.[4,5,7,54] The use of flux solvents or eutectics that contain borates, phosphates, or silicates are typically avoided owing to the fact that these covalent anion groups easily form highly viscous liquids and vitreous phases.[4] Many additional types of molten salts that have been reported in the literature for the growth of crystals include peroxides, chalcogenides, chalcophosphates, hydrofluxes, or metals/intermetallics, with each of these being system specific.[4,7,64–72]

One limitation in the use of molten-salt fluxes is that it is desirable for them to not react with the reaction container and to not be incorporated into the final products. For example, alkali- or alkaline-earth-metal hydroxides and lead(II) oxide fluxes are extensively used to solubilize reactants due to their high oxobasicity, and have especially been shown to corrode alumina and platinum crucibles, respectively. Corrosion of the reaction containers can cause aluminum or platinum contamination; therefore, care should be taken when using these materials as fluxes.[7] In order to minimize the incorporation of the flux ions into the crystalline products, it is typical to select a molten-salt flux with common cations or anions as that of the targeted product.[1–3,7,8] For example, the flux synthesis of Cu(I)-containing mixed-metal oxides (e.g., $CuNb_3O_8$, $Cu_2Nb_8O_{21}$, $Cu_5Ta_{11}O_{30}$, $Cu_3Ta_7O_{19}$, etc.) react with alkali-metal salts results in the formation of well-known phases such as $NaBO_3$ and $Na_2B_4O_{11}$ (B = Nb, Ta), and hence must be prepared using a CuCl flux solvent.[15,16,19,21,38,73–77] There are cases in which the flux may take on the role of a reagent in a beneficial manner for ion-exchange methods, as will be discussed later.

B. SYNTHETIC CONDITIONS FOR FLUX SYNTHESIS

The solubility of the reagents and the optimum growth rate of the crystalline product is system specific, and therefore tuning the flux ratios and cooling times are paramount to avoiding dendritic growth (too much flux) or agglomerate growth (too little flux). The resulting crystal size is a function of the degree of supersaturation of the flux solution, where reaching optimal supersaturation aids in minimizing the presence of crystal defects at the surfaces.[1–3,7] Flux-to-reactant molar ratios are instrumental in adjusting the concentration of reactants in the molten salt over a wide range, typically from 1:1 to 50:1 molar ratio. Modifying the flux-to-reactant molar ratio can be used to improve the reaction rate and solubility in order to yield well-defined single-crystal particles. The reaction temperatures, times, and cooling rates all can be varied quite significantly. Reaction temperatures just above that of the melting point of the flux are typically used for crystal growth, but reaction temperatures can range from two-thirds of the melting point to 100-400 °C above the melting point. The reaction temperature should be well below that of the boiling point of the flux in order to avoid volatilization.

In order to nucleate larger well-defined crystals, slower cooling rates are usually used and can vary between 1 to 60 °C per hour. Quenching of the flux mixture has been shown to yield single crystals as well, but typically of smaller sizes. The mixture is brought above the melting point of the flux and soaked at that temperature typically for 15 min to 120 h in order to enable dissolve the reagents and saturate the molten-salt mixture. Depending on the chemical system, slow cooling or quenching can cause the molten flux to supersaturate. Supersaturation is favorable for crystal nucleation and subsequent growth once a critical size has been reached.[7] Recent flux syntheses of Cu(I) niobates using a CuCl flux has been shown to yield, after quenching, well-defined platelet crystals for $CuNb_3O_8$ (750 °C for 15 min; quench) and rod-shaped crystals for $Cu_2Nb_8O_{21}$ (550 °C for 24 h; quench), as shown in Figure 2.[15,38]

C. FLUX SYNTHESIS OF METAL-OXIDE NANOPARTICLES

The nanostructuring of ternary and quaternary metal-oxides using a molten flux has proven to be synthetically challenging within many chemical systems. Early investigations into the flux synthesis of nanoparticulate $BaTiO_3$ crystals have led to the development of viable approaches for the nanoscaling of mixed-metal oxides.[34,78–81] Selective growth of mixed-metal oxide nanoparticles can be accomplished using i) lower reaction temperatures, ii) short reaction times with quenching of the reaction mixture, iii) nanoparticulate precursors with desired particle shapes, and iv) increased dissolution rates of precursors by adjusting the flux conditions. The dissolution rates of the precursors can be controlled by following the solubility rules given by the Lux-Flood and HSAB theories. These guidelines have been the driving force for the growth of mixed-metal oxide nanocrystals, such as $Cu_2Nb_8O_{21}$,[15] $ATiO_3$ (A = Sr, Ba, Pb),[13,78–82] $ANbO_3$ (A =Li, Na, K),[83–85] $LaMnO_3$,[78] $BaTi_2O_5$,[86] Sr_2SbMnO_6,[87] and for several Li-ion battery materials.[59,88–91] In all cases, the initial sizes and morphologies of the less soluble metal-oxide precursors (e.g., TiO_2, Nb_2O_5) have largely determined the morphology and nanoscale dimensions of the desired products, such as nanoparticulate rods, spheres, cubes, platelets, and wires. Synthetic modulation of the particle characteristics can also have a large impact on metal-oxide surfaces that influence their photocatalytic properties, as described below.

V. USE OF FLUX REACTIONS IN PHOTOCATALYTIC INVESTIGATIONS

Flux-preparation of metal-oxides has been of increasing importance in a growing number of studies probing photocatalysis mechanisms and surface reactivities of metal-oxide photocatalysts.[12,13,19,21,23–25,30] Flux crystal growth of complex metal-oxide photocatalysts is a growing focus of new investigations compared to commonly used binary oxides (e.g., TiO_2, NiO) as a result of the new capability to tune electronic configurations and optical bandgap sizes. Each metal-oxide has its own unique crystal growth conditions based on the reagents used, choice of flux solvent, and the synthetic conditions; therefore, no broad generalization on the design strategy, growth mechanism, or particle formation can be assumed for all flux reactions. As described below, each of these particle characteristics has been shown to play a significant role in governing the photocatalytic reaction rates at the surfaces of metal oxides.

A. PHOTOCATALYTIC REACTIONS OF METAL-OXIDE PARTICLES

As described in many recent reviews, the photocatalysis of suspended metal-oxide particles is driven by the absorption of photons and the separation of the excited electron-hole pairs within the depletion layer at the particles' surfaces,[92] as illustrated in Figure 3. Suspended particle photocatalysis for water-splitting can be described as a three step process, i) the absorption of photons greater than the band gap energy, ii) charge separation followed by migration of photogenerated carriers to the surfaces, and iii) reaction of the carriers with adsorbed chemical species at the surface.[93,94] At the solid-solution interface band bending within the depletion layer of the photocatalyst is caused by the charge transfer between the solution and the metal-oxide until the Fermi levels have equilibrated.[92,95] The depth of this depletion region is referred to as the space charge width (W), and the electric field established within this region is responsible for driving the electron-hole separation. The space charge width is determined by a number of parameters, as shown in Figure 3, including the dielectric constant (ε_r), dopant density (N_D), and space charge height (ϕ_{SC}).[95,96] The excited charge carriers are separated and driven to the particles' surfaces where reduction and oxidation reactions of surface species can occur, for example, in the reduction and/or oxidation of water to hydrogen and oxygen gas. Electron-hole recombination will predominate when the photon is absorbed deeper within the bulk of the particle beyond the space charge layer. Metal-oxides with an optimal match of their space charge widths to their single-crystal particle sizes and shapes are expected to yield the most efficient photocatalytic activity. In addition, factors such as crystallinity and exposed surface facets can play a predominant role in affecting the photocatalytic activity of metal-oxide particles.

Cocatalysts deposited on the surfaces of metal oxides act as enhanced active sites for water oxidation and reduction as a result of the ohmic contact established at the metal-semiconductor interface.[95,97–100] The roles that increased crystallinity and particle surfaces have in the enhancement of photocatalytic efficiencies are revealed by the preferential deposition of cocatalysts at the particles' surfaces. Investigations have shown that cocatalysts such as Pt and RuO_2 preferentially deposit at well-defined surface features (e.g., steps, edges, corners, etc.) of metal-oxide particles.[13,23,24,26,99,100] These surface features are the preferred active sites for electron migration to the solid-solution interface for the formation of catalytic products (e.g., H_2 and O_2). The increased crystallinity of metal-oxide particles prepared from flux methods can reduce defect sites present in the bulk and at the surface that can lead to electron-hole recombination, subsequently increasing the overall photocatalytic activity.[92,94,101]

B. EFFECTS OF PARTICLE MORPHOLOGIES, SIZES, AND SURFACES ON PHOTOCATALYTIC REACTION RATES

Early investigations into the photocatalytic activities of metal oxides utilized only high-temperature ‘grind and heat’ solid-state syntheses to obtain the desired products.[28,102–105] Starting with research by the Maggard group, the flux syntheses of metal-oxide photocatalysts with synthetic tunability have been used increasingly to understand the impact of the particle sizes, morphologies, and the underlying crystal structure.[3,7,24,29,92,101] For example, the solid-state preparation of the layered perovskite $La_2Ti_2O_7$ was previously found to exhibit a quantum efficiency of 27% for hydrogen production from aqueous solutions under ultraviolet-light irradiation.[25] However, using a eutectic Na_2SO_4/K_2SO_4 (1:1 molar ratio) flux, the $La_2Ti_2O_7$ particle sizes could be tuned by varying the reaction times and flux-to-reactant molar ratios. The Na_2SO_4/K_2SO_4 eutectic flux has been found to be useful for obtaining well-defined particle shapes owing to its Lux-Flood oxobasicity and reduced melting point. Anisotropic platelet-like morphologies were produced with minimum lateral dimensions of ~500 nm and platelet thicknesses of ~100 nm. The measured photocatalytic rates for hydrogen formation for the flux-synthesized $La_2Ti_2O_7$ powders increased with decreasing particle sizes, exhibiting a maximum rate of ~140 μmol $H_2 \cdot g^{-1} \cdot h^{-1}$. These rates were up to two times greater than the solid-state prepared sample, which exhibited a lower rate of ~87 μmol $H_2 \cdot g^{-1} \cdot h^{-1}$, owing to the platelets having an increased active surface area and smaller particle size.[25] Particles with nanoscale dimensions have an increased total surface area with shorter carrier migration distances, providing a larger number of available reaction sites at the surface. Thus, flux reaction conditions can be instrumental in optimizing the surface-to-volume ratio of single-crystal particles (i.e., with nanosized dimensions) in order to maximize the photocatalytic rates.[92,101]

Among the most active photocatalysts, the 2% La-doped $NaTaO_3$ has been found to exhibit the highest reported quantum efficiency (~56% at 270 nm). This has been attributed to surface nanostepped structures on its single-crystal particles that are 0.1 – 0.7 μm in height as a result of lanthanum doping.[21] By comparison, non-doped $NaTaO_3$ particles, with sizes of 2–3 mm and flat surfaces, show decreased rates by a factor of four times or more. The nanostepped surfaces of La-doped $NaTaO_3$ create both a higher surface area as well as separate surface sites for H_2/O_2 production that help inhibit recombination and back reactions. Using flux synthetic methods, La-doped $NaTaO_3$ can be prepared within a Na_2SO_4/K_2SO_4 eutectic flux. Particle sizes were tuned by a factor of up to two to three times by varying the flux-to-reactant molar ratio, and also producing particles with nanostepped surface features.[21] However, smaller particle sizes resulted in decreased photocatalytic rates for H_2 production of ~30-40%. Reduction in the photocatalytic rates are attributed to the potential gradient within the space charge region, which is typically negligible when the dimensions of the crystal are much smaller than twice the width of the space charge region (e.g., estimated at ~100 to 200 nm for La-doped $NaTaO_3$). As a result, the rate of electron-hole recombination increases when the particles' dimensions are modified to significantly less than that of the space charge width.[92,95,101] Similar results have been found for $AgNbO_3$ and $PbTiO_3$, both of which exhibit higher photocatalytic rates for H_2 and/or O_2 formation for the larger particle sizes obtained from flux methods. However, their photocatalytic rates for hydrogen production were up to twice as much as compared to the same products obtained using solid-state methods. The increase in photocatalytic rates as a result of using a flux has been attributed to the well-defined surface features that serve as active sites for photocatalytic water splitting.[12,13,24,25]

The exposed crystallographic facets of metal oxides can be varied as a result of growing different particle morphologies, such as rods, platelets, cubes, octahedrons, or related intermediate shapes using flux methods.[3,7,13,23,24,29] In recent research, Kakihana et al. have shown that the particle morphologies, sizes, and exposed crystal facets of $SrTiO_3$ are highly dependent on the choice of flux, and have a significant impact on the photocatalytic activities. The $SrTiO_3$ phase was prepared by both solid-state and flux methods at 1000 °C using LiCl, NaCl, KCl, and $SrCl_2$ fluxes in a 1:1 flux-to-reactant molar ratio, resulting in single-crystal particles shown in Figure 4. The alkali-metal halide fluxes were unreactive, acting purely as a solvent system and avoiding the formation of undesired by-products (i.e., $ATiO_3$; A = Li, Na, K). The metal halide fluxes can act as mineralizers, with the varied cation sizes effecting the melting point, viscosity, and supersaturation of the flux solvent system in order to yield various well-defined particle shapes. By contrast, solid-state methods yielded irregularly-shaped particles that were largely aggregated with sizes of ~5-15 μm for the agglomerates. The LiCl flux yielded large cubes with sizes of ~5-6 μm with primarily {100} exposed crystal faces. The use of a NaCl or $SrCl_2$ flux yielded edge-truncated cubic-shaped particles with sizes of ~300 nm and {100} and {110} exposed crystal faces. The KCl flux-prepared particles were of comparable sizes, but with highly-faceted particle morphologies. The KCl flux resulted in particles with the {100}, {120}, and {121} crystal faces exposed at their surfaces and smaller particles sizes that yielded significantly enhanced photocatalytic rates of ~6.6 mmol $H_2 \cdot g^{-1} \cdot h^{-1}$ and ~3.3 mmol $O_2 \cdot g^{-1} \cdot h^{-1}$.[29]

A recent investigation by Takanabe et al. into the flux synthesis of the $SnNb_2O_6$ photocatalyst demonstrates the utility in tuning flux-to-reactant molar ratios for optimizing particle sizes and photocatalytic activities. The $SnNb_2O_6$ compound was prepared at 600 °C using a $SnCl_2$ flux at various flux-to-reactant molar ratios, resulting in platelet-shaped morphologies. The $SnCl_2$ flux solvent has a common Sn(II) cation and was found to have a mineralizing effect. By contrast, conventional solid-state methods resulted in irregularly-shaped agglomerated particles, as shown in Figure 5. Increases in the flux-to-reactant molar ratio led to anisotropic crystal growth along the lower energy *bc* plane at a slower growth rate and afforded well-faceted and smooth platelet morphologies with {00*l*} exposed crystal faces. An increase in particle size from ~0.3 to ~3.0 µm was observed with an increase in the flux ratio. As the particle sizes increased as a function of the flux ratio, the photocatalytic rates for hydrogen production as well increased from ~244 to ~316 µmol $H_2 \cdot g^{-1} \cdot h^{-1}$.[20] The increased photocatalytic activity for hydrogen production was also attributed to the decrease in Sn(IV) surface defects and the highly-faceted surfaces of the flux-prepared particles. The flux preparation minimized the number of surface defects and grain boundaries that can act as electron-hole recombination sites, which are found in higher amounts in agglomerated particles resulting from solid-state preparations.[20]

Structures with layered metal-oxide connectivity, as shown in Figure 6 for Dion-Jacobsen and Ruddlesden-Popper phases, show significantly higher charge mobility along the two-dimensional layers of their structures. Single-crystal particles of these perovskite structures also most commonly grow as platelets with the metal-oxide layers parallel to the plane of the platelets. For example, the Dion-Jacobsen $RbLaNb_2O_7$ phase could be prepared in the form of thin platelet morphologies from a RbCl flux, with lateral dimensions of several micrometers and platelet thicknesses of ~100 to ~300 nm. The RbCl salt was utilized as a flux due to its low melting point, mineralizing effect, and the Rb(I) cation common between the flux and $RbLaNb_2O_7$ product. The photocatalytically-active surface sites of the platelets were observed to be at the particle edges and surface steps, as found by using the photochemical reduction reaction of Pt(s) islands at the surfaces as chemical ‘markers’ of surface reaction sites, as shown in Figure 7. Platinum surface cocatalysts act as active sites for photocatalytic water splitting. Therefore, the active sites of metal-oxide particles can be inferred by the location of the platinum surface islands. Electronic structure calculations on $RbLaNb_2O_7$ confirmed that the excited electrons are preferentially confined to the metal-oxide layers along the lateral dimensions of the particles, until reaching a surface step or edge to drive reduction reactions. In another example, the Ruddlesden-Popper $Na_2Ca_2Nb_4O_{13}$ layered phase could be flux-prepared as large micrometer to millimeter-sized platelets within a Na_2SO_4 molten salt at 1100 °C, as shown in Figure 8. The Na_2SO_4 oxosalt flux was utilized due to its previous success in other reactions, its Lux-Flood oxobasicity, and the Na(I) cation common in the flux and $Na_2Ca_2Nb_4O_{13}$ product. Increasing the amount of flux yielded the larger particle sizes and the highest photocatalytic activities for hydrogen formation from aqueous solutions of ~447 $\mu mol\ H_2 \cdot g^{-1} \cdot h^{-1}$. The surfaces of the larger platelets had a larger concentration of stepped features at the edges that were ~10-120 nm in height, and where the Pt(s) islands preferentially deposited.[23] Surface absorption of molecular species, and their catalytic reactivity, is well known to occur most favorably at surface features like steps, edges, corners, etc.[19,23,24,26]

Flux synthetic techniques can also be utilized to modify the particle morphology, e.g., from the platelet-shaped to rod-shaped crystal morphology shown in Figure 8. For example, the synthesis of $Na_2Ca_2Nb_4O_{13}$ using a NaCl flux yielded ~1-10 μm long rod-shaped particles, rather than the more common platelet morphologies. The NaCl flux was utilized due to the lower melting point compared to Na_2SO_4, mineralizing effect, and the Na(I) cation common between the NaCl flux and $Na_2Ca_2Nb_4O_{13}$ product. The NaCl flux solvent will differ in viscosity and growth rate, which led to the preferential growth of rod-shaped particles. The photocatalytic activity of $Na_2Ca_2Nb_4O_{13}$ prepared using a NaCl flux was 1,355 μmol $H_2 \cdot g^{-1} \cdot h^{-1}$; significantly higher than that obtained from the platelet morphologies using a Na_2SO_4 flux. For the rod-shaped morphology, the higher surface areas of the smaller particles resulted in an increase in the photocatalytic activities for hydrogen formation in aqueous solutions. The rod-shaped particles also possessed a shorter diffusion length for the excited electrons to migrate and react at the surfaces, such as depicted in Figure 3. The change in morphology from platelet-shaped to rod-shaped particles is useful in order to adjust for a larger or smaller space charge width, respectively. Modification of the particle morphologies also aids in orienting the structural features that yield higher charge mobility (e.g., along extended metal-oxide layers) along either the short or long dimensions of the single crystal particles. Adjusting the choice of flux, flux-to-reactant molar ratio, and reaction time and temperature can be used to achieve rod- and platelet-shaped morphologies, as shown for $PbTa_4O_{11}$[27] and $RbLaNb_2O_7$[24], respectively, in Figure 9. Similar investigations into the impact of flux synthesis on particle morphologies and photocatalytic activities have been reported for many metal-oxide photocatalysts, such as $PbTiO_3$, $AgNbO_3$, and $Na_2Ta_4O_{11}$.[12,13,19,21,24,25]

VI. FLUX SYNTHESIS OF NEW METAL-OXIDES FOR PHOTOCATALYSIS RESEARCH

Molten-salt flux techniques can also be used in the preparation of new metal-oxides with desired compositions and structures. Flux reactions can provide access to the crystal growth of new compositions, structures, and morphologies of phases that have not been previously achieved using traditional solid-state methods. Flux synthesis can also aid in thermodynamically or kinetically stabilizing new phases during crystal growth by increasing the lifetimes of the nonequilibrium phases.[106,107]

A. FLUX-MEDIATED ION-EXCHANGE REACTIONS

The flux-mediated exchange reaction involves the use of pre-synthesized metal-oxides with a desired parent structure, and its reaction within a low-temperature molten-salt flux. The flux-exchange method has some distinct advantages over using binary-oxide starting materials. In this method the molten-salt takes on the role of a reagent by exchanging its cations with those within the metal-oxide structure. The ion-exchange reaction incorporates the cations from the salt into the crystal structure of the metal-oxide while maintaining the desired parent structure, in order to yield new compositions.[7,26,108,109] The reaction is facilitated by the dissolution of the cations between the metal-oxide layers and the subsequent cation exchange in the molten flux. Selectivity for ion-exchange is observed in molten salts based on ion solubility, with smaller crystal radii being preferred ion-exchangers.[110–112] Ion-exchange reactions have been previously investigated by ex-situ PXRD analyses,[113] and have been found to proceed by more than a simple two-phase process, but rather with several intermediate complex phases. An intermediate phase forms almost immediately in a molten flux, with extremely fast exchange kinetics, followed by a slower phase conversion as the ions re-order. The intermediate phases contain randomly distributed mixtures of cations from the flux and those from the parent phase. For example, studies of the Na-exchange of $LiNi_{0.5}Mn_{0.5}O_2$ were found to exhibit two intermediate phases, $Na_{0.19}Li_{0.66}Ni_{0.5}Mn_{0.5}O_2$ and $Na_{0.29}Li_{0.53}Ni_{0.5}Mn_{0.5}O_2$, before forming the $NaNi_{0.5}Mn_{0.5}O_2$ phase. The slower phase conversion prevents the collapse of the interlayer space and facilitates the formation of the ion-exchanged phase.[113] This method overcomes common issues with binary-oxide mixtures that melt incongruently and that may favor a different composition for nucleation.[7]

Metal oxides with layered structural features have been shown to exhibit ion-exchange behavior of their interlayer cations in the molten solvent.[24,26,27,30,32,94,108,109,114–117] The layered Dion-Jacobson (DJ) and Ruddlesden-Popper (RP) perovskite phases have especially been shown to exhibit facile ion-exchange of their interlayer cations. The general formulas for the DJ and RP phases are $A'[A_{(n-1)}B_nX_{(3n+1)}]$ and A_2' $[A_{(n-1)}B_nX_{(3n+1)}]$, respectively, where the A'-sites are the interlayer cations (e.g., A' = Na, K, Rb), the A-site cations are located within the layers (e.g., A = La, Ca, Sr), and *n* defines the octahedral layer thickness ($n = 2, 3$) of the B-site cations (e.g., B = Ti, Nb, Ta).[24,26,32,94,109,114,116] Exchange reactions with layered perovskites may occur without alteration of adjacent oxide layers, with the structure differing only in their interlayer separations. Some of the perovskites that have been reported to exhibit this ion-exchange behavior are $KCa_2Nb_3O_{10}$, $K_2La_2Ti_3O_{10}$, and $RbLaNb_2O_7$, as shown in Figure 6 and listed in Table 1.[24,26,32,108,114–116,118] The interlayer cations have been reported to be exchanged for other alkali-metals (e.g., Li, Na, K, Rb, Cs) and transition metals (e.g., Ag, Cu).[24,26,114–116,118–120] The flux exchange of these interlayer cations not only facilitate the synthesis of new compositions and phases with limited stability, but can be used to tune optical, electronic, and photocatalytic properties of mixed-metal oxides.

Flux-exchange of alkali- and alkaline-earth metal cations within the parent structure with transition-metal cations, e.g., those with d^{10} (e.g., Ag(I) or Cu(I)) or $d^{10}s^2$ electron configurations (e.g., Pb(II) or Bi(III)), has yielded metal oxides with visible-light band gap energies.[15,24,28,32,109,116] Transition metals with filled d^{10} or $d^{10}s^2$ orbitals can result in higher energy valence bands (i.e., shifted to a less positive potential), while the conduction band remains comprised of transition metals with empty d orbitals (e.g., Ti(IV), Nb(V), and Ta(V)). This can effectively decrease their bandgap sizes in order to sensitize the structure to the absorption of visible-light. Increased absorption of the full solar spectrum aids the photocatalyst in reaching the maximum possible solar efficiency.[24,30] Recently, many mixed-metal oxides containing two transition metals with d^0 and d^{10} or $d^{10}s^2$ electron configurations have shown high activities for water-splitting reactions under only visible-light irradiation.[24,94]

In recent research, the optical absorption and photocatalytic activities of metal oxides have been investigated with the use of a low-temperature $AgNO_3$ flux to yield silver-exchanged metal oxides. Silver-exchange reactions of the layered $RbLaNb_2O_7$, $RbA_2Nb_3O_{10}$ (A = Ca, Sr), and $Rb_2La_2Ti_3O_{10}$ perovskite structures were found to yield the $AgLaNb_2O_7$, $AgA_2Nb_3O_{10}$ and $Ag_2La_2Ti_3O_{10}$ phases that exhibited a pronounced red-shift in the optical absorption edge by ~0.5 to ~1.0 eV. After the silver-exchange reactions, the particles were shown to maintain their original morphologies and sizes, as shown in the SEM images in Figure 7 for $RbLaNb_2O_7$ and $AgLaNb_2O_7$. Electronic structure calculations confirmed the formation of a new higher-energy valence band comprised primarily of the Ag $4d^{10}$ orbitals in each of these layered structures. All silver-exchanged products exhibited significant increases in their photocatalytic rates for hydrogen production. The silver-exchanged $RbA_2Nb_3O_{10}$ structures, i.e., $AgA_2Nb_3O_{10}$, exhibited the largest increase in the photocatalytic rates for hydrogen production in aqueous methanol under ultraviolet and visible irradiation (~13,616 μmol $H_2 \cdot g^{-1} \cdot h^{-1}$) compared to before silver-exchange (~1,418 μmol $H_2 \cdot g^{-1} \cdot h^{-1}$).[24,26] The photocatalytic rates were also found to increase exponentially over time as the Ag(I) cations deposited on the surfaces and interlayer spacings as Ag(s) nanoislands to act as cocatalysts.[26]

Ternary tantalates and niobates of the $A^{m+}_{(n+1)/m}B_{3n+1}O_{(8n+3)}$ (A^{m+} = Na(I), Ag(I), Cu(I), Pb(II); B = Nb, Ta) structural family can be prepared by exchange of the A-site cations using a molten flux. For example, the hexagonal lead-tantalate phases $Pb_{1.5}Ta_7O_{19}$ and $PbTa_4O_{11}$ were discovered by flux-mediated lead-exchange reactions starting from the $Cu_3Ta_7O_{19}$ and $A_2Ta_4O_{11}$ (A = Na, Ag) parent structures and a $PbCl_2$ flux at 800 °C and 700 °C, respectively. These lead tantalate phases could only be achieved by lead-exchange reactions using a $PbCl_2$ flux in vacuum sealed fused-silica tubes. Solid-state syntheses and lead-exchange reactions of $A_2Ta_4O_{11}$ (A = Na, Ag) using $PbCl_2$ in air instead yielded the $PbTa_2O_6$ and $Pb_3Ta_4O_{13}$ phases, respectively.[27,117] Lead-exchange reactions under vacuum and in air yielded rod- and octahedron-shaped morphologies for $PbTa_4O_{11}$ and $Pb_3Ta_4O_{13}$ phases, respectively. The slow growth of $A^{m+}_{2/m}Ta_4O_{11}$ along the *c* axis results in rod-shaped particles, as shown in Figure 10. The $PbTa_4O_{11}$ phase exhibited a bandgap size of ~3.8 eV,[27] which is ~0.5 eV smaller in energy than that found for $Na_2Ta_4O_{11}$ at ~4.3 eV.[19] A reduction in the band gap was also observed with an increase in the Pb(II) content as a result of the flux exchange, and which served to increase the photocatalytic activities for hydrogen and oxygen production. The $PbTa_4O_{11}$ phase was reported with a photocatalytic activity of ~175 µmol $H_2 \cdot g^{-1} \cdot h^{-1}$ in aqueous methanol under ultraviolet and visible irradiation, while the solid-state prepared precursor $Ag_2Ta_4O_{11}$ had a rate of ~23 µmol $H_2 \cdot g^{-1} \cdot h^{-1}$. The $PbTa_4O_{11}$ phase generated ~181 µmol $O_2 \cdot g^{-1} \cdot h^{-1}$ in aqueous silver nitrate under ultraviolet and visible irradiation, while its precursor $Ag_2Ta_4O_{11}$ exhibited a similar rate of ~165 µmol $O_2 \cdot g^{-1} \cdot h^{-1}$. Higher activity for water reduction was reported for layered tantalate structures comprised of TaO_7 pentagonal bipyramid layers, which can serve as extended charge-migration pathways.[27]

B. PREPARATION OF METAL-OXIDES WITH LIMITED STABILITY

The synthesis of metastable metal-oxides in high purity is challenging using conventional solid-state synthesis techniques. Metastable phases are formed due to the stabilization of a higher-energy phase when the chemical system cannot reach equilibrium at the timescale afforded by the reaction conditions. A finite energy barrier for the diffusion of ions can hinder the transformation of the system from a higher-energy phase into a more energetically stable phase. At high temperatures there is a higher probability of transforming into the most stable phase, and so there is a characteristic "lifetime" for a metastable phase. Compositional, structural, and morphological metastable phases form under non-equilibrium and kinetically-controlled pathways.[106,107] An optimal temperature range where nucleation rates are at their maximum for metastable phases exists and can be extended by modifying the crystal growth rate. The rate of crystal growth is a function of the concentration and viscosity of the solution, which is dependent on the flux used. A critical size during nucleation must be achieved in order to facilitate the growth of metastable phases, which can occur if isolated during its finite lifetime.[7,106,107,111] Use of a molten salt as a flux for the synthesis of metal oxides increases the temperature range and lifetime of the metastable phase, facilitating rapid crystal growth.[1]

Several Cu(I)-containing mixed-metal oxides are reported to exist in the Cu_2O-M_2O_5 (M = Nb,Ta) system that cannot be synthesized using conventional solid-state methods.[121] For example, the synthesis of $Cu_2Nb_8O_{21}$, a metastable *p*-type semiconductor, was prepared in high purity by the reaction of Cu_2O and Nb_2O_5 nanoparticles within a CuCl flux using a 10:1 flux-to-reactant molar ratio.[15] The CuCl flux solvent was preferentially utilized in these reactions owing to its low melting point, ability to solubilize Cu_2O, and the common Cu(I) cations as that of the Cu_2O reagent. The reaction mixture was heated in an evacuated fused-silica ampoule at 550 °C for 24 h that was immediately quenched.[15] The $Cu_2Nb_8O_{21}$ phase does not form in the absence of a molten flux at lower temperatures of 550 °C. At a higher reaction temperature of 650 °C the $Cu_2Nb_8O_{21}$ compound begins to transform into $CuNb_3O_8$, and after the temperature reaches 750 °C, the $Cu_2Nb_8O_{21}$ compound has completely transformed into $CuNb_3O_8$. In the Cu_2O-Ta_2O_5 system, the $Cu_2Ta_4O_{11}$ and $Cu_7Ta_{15}O_{41}$ phases have not been reported to have been synthesized in high purity, but instead have been found as side products at reaction temperatures ranging from 700 °C to 1000 °C.[122] Both the $Cu_2Ta_4O_{11}$ and $Cu_7Ta_{15}O_{41}$ phases have been calculated to have 33% and 22% vacancies on the copper-site positions within the unit cell, respectively. The $Cu_2Ta_4O_{11}$ phase has been reported to be stabilized through doping with zirconium and by utilizing solid solutions such as $Cu_{2-x}Na_xTa_4O_{11}$.[76,123] These Cu(I)-containing mixed-metal oxides exhibit band gaps deep within the visible-light energy range, spanning from ~1.3 eV to ~2.6 eV, and have shown high cathodic photocurrents for water reduction under visible-light in the form of polycrystalline photoelectrodes. Thus, the preparation of new Cu(I)-oxides in high purity can be facilitated with the use of a flux-mediated synthetic route in combination with binary-oxide nanoparticle precursors.

Phases containing transition-metal cations with higher oxidation states (e.g., $LaFeO_3$) can be stabilized by superoxides and peroxides that form in alkali-metal hydroxide fluxes at lower reaction temperatures, e.g., NaOH-KOH eutectic.[4,5,7,22,31,54,56,57,59,60,90,124–126] The crystalline rare-earth orthoferrites $LnFeO_3$ (Ln = La, Pr, Nd) have been synthesized by flux methods at a temperature of 400 °C using a molten hydroxide in a 10:1 flux-to-reactant molar ratio.[22] The syntheses of the $LnFeO_3$ phases were attempted by means of a eutectic NaOH–KOH flux with a heating temperature of 300-500 °C and a reaction time of 6-24 h. The hydroxide eutectic flux has a reduced melting point and increased oxobasicity from incorporating KOH. These reaction conditions did not yield a phase-pure product; therefore the syntheses were attempted via a pure NaOH or KOH flux. Phase-pure $LnFeO_3$ products were formed using a NaOH flux, but the metastable phases were not observed when using only a more basic molten KOH flux. The flux preparation using a NaOH flux yielded crystals with sizes of 5–10 μm and a cube morphology indicative of growth along the {100}, as shown in Figure 11.[22]

VII. SUMMARY AND OUTLOOK

Flux-mediated crystal growth is an ideal method as a result of its synthetic flexibility and capabilities in obtaining well-defined single-crystal particles and surface structures. Flux methods used in conjunction with nanoparticle reagents may be used in order to obtain nanocrystalline mixed-metal oxides for better synthetic control over particle morphologies, sizes, and surface features for enhanced photocatalytic activities. Compositional modifications of flux-prepared mixed-metal oxides can effectively decrease the band gap energy in order to sensitize photocatalysts for visible-light absorption in order to reach maximum solar efficiency. Tremendous advances in the flux crystal growth of mixed-metal oxides for practical applications in photocatalysis research have made them a viable alternative to commonly utilized binary oxides such as TiO_2 and NiO. Further modifying flux methods for tuning particle sizes, morphologies, specific surface areas, and crystallinity can be used in order to obtain nanoparticulate mixed-metal oxides that can have highly desired optical and photocatalytic properties.

VIII. REFERENCES

(1) Elwell, D.; Neate, B. W. *J. Mater. Sci.* **1971**, *6*, 1499.

(2) Elwell, D.; Scheel, H. J. *Crystal Growth from High-Temperature Solutions*; Academic Press Inc.: New York, NY, 1975; pp. 4–5.

(3) Kimura, T. In *Advances in Ceramics - Synthesis and Characterization, Processing and Specific Applications*; Sikalidis, C., Ed.; InTech, 2011; pp. 75–100.

(4) Liu, X.; Fechler, N.; Antonietti, M. *Chem. Soc. Rev.* **2013**, *42*, 8237.

(5) Mugavero, S. J.; Gemmill, W. R.; Roof, I. P.; zur Loye, H.-C. *J. Solid State Chem.* **2009**, *182*, 1950.

(6) Yan, B.; Lei, F. *J. Alloy. Compnd.* **2010**, *507*, 460.

(7) Bugaris, D. E.; zur Loye, H.-C. *Angew. Chem., Int. Ed.* **2012**, *51*, 3780.

(8) Corbett, J. D. In *Survey of Progress in Chemistry, Vol. 2*; Academic Press: New York, 1964; pp. 91–154.

(9) Smart, L. E.; Moore, E. A. *Solid State Chemistry: An Introduction*; Third Edit.; Taylor & Francis: Boca Raton, FL, 2005; pp. 125–153.

(10) Venkatesan, T. V.; Blamire, M. *Functional Metal Oxides: New Science and Novel Applications*; Ogale, S. B., Ed.; Wiley-VCH: Weinheim, Germany, 2013; pp. 12–14.

(11) Ebrahimi, M. E.; Allahverdi, M.; Safari, A. *J. Am. Ceram. Soc.* **2005**, *88*, 2129.

(12) Arney, D.; Hardy, C.; Greve, B.; Maggard, P. A. *J. Photochem. Photobiol., A* **2010**, *214*, 54.

(13) Arney, D.; Watkins, T.; Maggard, P. A. *J. Am. Ceram. Soc.* **2011**, *94*, 1483.

(14) Bondioli, F.; Bonamartini Corradi, A.; Leonelli, C.; Manfredini, T. *Mat. Res. Bull.* **2000**, *34*, 2159.

(15) Choi, J.; King, N.; Maggard, P. A. *ACS Nano* **2013**, *7*, 1699.

(16) Fuoco, L.; Joshi, U. A.; Maggard, P. A. *J. Phys. Chem. C* **2012**, *116*, 10490.

(17) Fuoco, L.; Rodriguez, D.; Peppel, T.; Maggard, P. A. *Chem. Mater.* **2011**, *23*, 5409.

(18) Giaquinta, D. M. *Chem. Mater.* **1994**, 365.

(19) Mclamb, N.; Sahoo, P. P.; Fuoco, L.; Maggard, P. A. *Cryst. Growth Des.* **2013**, *13*, 2322.

(20) Noureldine, D.; Anjum, D. H.; Takanabe, K. *Phys. Chem. Chem. Phys.* **2014**, *16*, 10762.

(21) Porob, D. G.; Maggard, P. A. *J. Solid State Chem.* **2006**, *179*, 1727.

(22) Shivakumara, C. *Solid State Comm.* **2006**, *139*, 165.

(23) Arney, D.; Fuoco, L.; Boltersdorf, J.; Maggard, P. A. *J. Am. Ceram. Soc.* **2013**, *96*, 1158.

(24) Arney, D.; Maggard, P. A. *ACS Catal.* **2012**, *2*, 1711.

(25) Arney, D.; Porter, B.; Greve, B.; Maggard, P. A. *J. Photochem. Photobiol., A* **2008**, *199*, 230.

(26) Boltersdorf, J.; Maggard, P. A. *ACS Catal.* **2013**, *3*, 2547.

(27) Boltersdorf, J.; Wong, T.; Maggard, P. A. *ACS Catal.* **2013**, *3*, 2943.

(28) Domen, K.; Yoshimura, J.; Sekine, T. *Catal. Lett.* **1990**, *4*, 1.

(29) Kato, H.; Kobayashi, M.; Hara, M.; Kakihana, M. *Catal. Sci. Technol.* **2013**, *3*, 1733.

(30) Porob, D. G.; Maggard, P. A. *Chem. Mater.* **2007**, 970.

(31) Roof, I. P.; Park, S.; Vogt, T.; Rassolov, V.; Smith, M. D.; Omar, S.; Nino, J.; Loye, H.; Gaines, V. *Chem. Mater.* **2008**, *20*, 3327.

(32) Takata, T.; Shinohara, K. *MRS* **1996**, *454*, 177.

(33) Jovilet, J. P. *Metal Oxide Chemistry and Synthesis*; 3rd ed.; Wiley: Paris, 2000.

(34) Einarsrud, M.-A.; Grande, T. *Chem. Soc. Rev.* **2014**, *43*, 2187.

(35) Geselbracht, M. J.; Noailles, L. D.; Ngo, L. T.; Pikul, J. H.; Walton, R. I.; Cowell, E. S.; Millange, F.; Hare, D. O. *Chem. Mater.* **2004**, 1153.

(36) Geselbracht, M. J.; Walton, R. I.; Cowell, E. S.; Millange, F.; Hare, D. O. *Chem. Mater.* **2002**, *14*, 4343.

(37) Gornert, P. *Prog. Cryst. Growth Charact.* **1990**, *20*, 263.

(38) King, N.; Sahoo, P. P.; Fuoco, L.; Stuart, S.; Dougherty, D.; Liu, Y.; Maggard, P. A. *Chem. Mater.* **2014**, *ASAP*.

(39) Burton, W. K.; Cabrera, N.; Frank, F. C. *Phil. Trans. R. Soc. Lond. A* **1951**, *243*, 299.

(40) Liu, Y.; Lu, Y.; Xu, M.; Zhoun, L. *J. Am. Ceram. Soc.* **2007**, *90*, 1774.

(41) Li, Z.; Zhang, X.; Hou, J.; Zhou, K. *J. Cryst. Growth* **2007**, *305*, 265.

(42) Porob, D. G.; Maggard, P. A. *Mat. Res. Bull.* **2006**, *41*, 1513.

(43) Cherginets, V. L. *J. Electroanal. Chem.* **2000**, *493*, 144.

(44) Cherginets, V. L.; Khailova, E. G. *Electrochim. Acta* **1994**, *39*, 823.

(45) Cherginets, V. L.; Rebrova, T. P.; Naumenko, V. a. *J. Chem. Thermo.* **2014**, *74*, 216.

(46) Ishitsuka, T.; Nose, K. *Corros. Sci.* **2002**, *44*, 247.

(47) Masset, P.; Guidotti, R. a. *J. Power Sources* **2007**, *164*, 397.

(48) Nakamura, S.; Iwasawa, K.; Morita, K.; Sano, N. *Met. Mater. Trans. B* **1998**, *29*, 411.

(49) Orfield, M. L.; Shores, D. A. *J. Electrochem. Soc.* **1989**, *136*, 2862.

(50) Qingfeng, L.; Borup, F.; Petrushina, I.; Bjerrum, N. J. *J. Electrochem. Soc.* **1999**, *146*, 2449.

(51) Skryptun, I. N. *ECS Trans.* **2010**, *33*, 303.

(52) Zinchenko, V. F.; Timukhin, E. V.; Pavlinchuk, S. a.; Nechiporenko, a. V.; Sadkovskaya, L. V. *Russ. J. Electrochem.* **2012**, *48*, 995.

(53) Byrappa, K.; Ohachi, T. *Crystal Growth Technology*; William Andrew Publishing: Norwich, New York, 2003.

(54) Flood, H.; Forland, T. *Acta Chem. Scand. B* **1947**, *1*, 592.

(55) Lux, H. *Z. Elektrochem. Angew. Phys. Chem.* **1939**, *45*, 303.

(56) Gemmill, W. R.; Smith, M. D.; zur Loye, H.-C. *J. Solid State Chem.* **2006**, *179*, 1750.

(57) Jagau, T.-C.; Roof, I. P.; Smith, M. D.; zur Loye, H.-C. *Inorg. Chem.* **2009**, *48*, 8220.

(58) Liao, J.; Leroux, F.; Payen, C.; Guyomard, D.; Piffard, Y.; K, Z. T. *J. Solid State Chem.* **1996**, *224*, 214.

(59) Liu, X.; Wu, J.; Huang, X.; Liu, Z.; Zhang, Y.; Wang, M.; Che, R. *J. Mater. Chem. A* **2014**, *2*, 15200.

(60) Mugavero III, S. J.; Smith, M. D.; zur Loye, H.-C. *J. Solid State Chem.* **2006**, *179*, 3586.

(61) Scheel, H. J.; Bednorz, J. G.; Dill, P. *Ferroelectrics* **1976**, *13*, 507.

(62) Yeon, J.; Hardaway, J. B.; Sefat, A. S.; Latshaw, A. M.; zur Loye, H.-C. *Solid State Sci.* **2014**, *34*, 24.

(63) Bale, C. W.; Bélisle, E.; Chartrand, P.; Decterov, S. a.; Eriksson, G.; Hack, K.; Jung, I.-H.; Kang, Y.-B.; Melançon, J.; Pelton, A. D.; Robelin, C.; Petersen, S. *CALPHAD* **2009**, *33*, 295.

(64) Canfield, P. C. In *Properties and Applications of Complex Intermetallics*; World Scientific Publishing Co.: Hackensack, NJ, 2009; pp. 102–121.

(65) Schmitt, D. C.; Kangas, M. J.; Chan, J. Y. *Mater. Matt.* **2011**, *6*, 1.

(66) Phelan, W. A.; Menard, M. C.; Kangas, M. J.; McCandless, G. T.; Drake, B. L.; Chan, J. Y. *Chem. Mater.* **2012**, *24*, 409.

(67) Kanatzidis, M. G. *Chem. Mater.* **1990**, *2*, 353.

(68) Kanatzidis, G. *Curr. Op. Solid State Mater. Sci.* **1997**, *2*, 139.

(69) Mccarthy, T. J.; Ngeyi, S.; Liao, J.; Degroot, D. C.; Hogan, T.; Kannewurf, C. R.; Kanatzidis, M. G. *Chem. Mater.* **1993**, *5*, 331.

(70) McCarthy, T. J.; Kanatsidis, M. G. *Chem. Mater.* **1993**, *5*, 1061.

(71) Willert, M.; Rothe, R.; Landfester, K.; Antonietti, M. *Chem. Mater.* **2001**, *13*, 4681.

(72) Chance, W. M.; Bugaris, D. E.; Sefat, A. S.; Loye, H. *Inorg. Chem.* **2013**, *52*, 11723.

(73) Joshi, U. A.; Palasyuk, A. M.; Maggard, P. A. *J. Phys. Chem. C* **2011**, *115*, 13534.

(74) Joshi, U. A.; Maggard, P. A. *J. Phys. Chem. Lett.* **2012**, *3*, 1577.

(75) Palasyuk, O.; Palasyuk, A.; Maggard, P. A. *J. Solid State Chem.* **2010**, *183*, 814.

(76) Palasyuk, O.; Palasyuk, A.; Maggard, P. A. *Inorg. Chem.* **2010**, *49*, 10571.

(77) Sahoo, P. P.; Maggard, P. A. *Inorg. Chem.* **2013**, *52*, 4443.

(78) Deloume, J.; Scharff, J.; Marote, P. *J. Mater. Chem.* **1999**, *9*, 107.

(79) Huang, K.-C.; Huang, T.-C.; Hsieh, W.-F. *Inorg. Chem.* **2009**, *48*, 9180.

(80) Li, B.; Shang, W.; Hu, Z.; Zhang, N. *Ceram. Int.* **2014**, *40*, 73.

(81) Zhang, Y.; Wang, L.; Xue, D. *Powder Technol.* **2012**, *217*, 629.

(82) Tian, X.; Li, J.; Chen, K.; Han, J.; Pan, S. *Cryst. Growth Des.* **2009**, *9*, 4927.

(83) Ge, H.; Hou, Y.; Xia, C.; Zhu, M.; Wang, H.; Yan, H. *J. Am. Ceram. Soc.* **2011**, *94*, 4329.

(84) Li, L.; Deng, J.; Chen, J.; Sun, X.; Yu, R.; Liu, G. *Chem. Mater.* **2009**, *21*, 1207.

(85) Santulli, A. C.; Zhou, H.; Berweger, S.; Raschke, M. B.; Sutter, E.; Wong, S. S. *CrystEngComm* **2010**, *12*, 2675.

(86) Yu, J.; Tang, S.; Wang, R.; Shi, Y.; Nie, B.; Zhai, L.; Zhang, X.; Du, Y. *Cryst. Growth Des.* **2008**, *8*, 1481.

(87) Baral, A.; Varma, K. B. R. *J. Solid State Chem.* **2009**, *182*, 3282.

(88) Liu, J.; Hou, M.; Yi, J.; Guo, S.; Wang, C.; Xia, Y. *Energy Environ. Sci.* **2014**, *7*, 705.

(89) Shi, S. J.; Tu, J. P.; Tang, Y. Y.; Liu, X. Y.; Zhao, X. Y.; Wang, X. L.; Gu, C. D. *J. Power Sources* **2013**, *241*, 186.

(90) Yu, C.; Li, G.; Guan, X.; Zheng, J.; Li, L. *J. Alloy. Compnd.* **2012**, *528*, 121.

(91) ZhenYao, W.; Biao, L.; Jin, M.; DingGuo, X. *Electrochim. Acta* **2014**, *117*, 285.

(92) Li, L.; Salvador, P. A.; Rohrer, G. S. *Nanoscale* **2014**, *6*, 24.

(93) Ismail, A. a.; Bahnemann, D. W. *Sol. Energy Mater. Sol. Cells* **2014**, *128*, 85.

(94) Osterloh, F. E. *Chem. Mater.* **2008**, *20*, 35.

(95) Zhang, Z.; Yates, J. T. *Chem. Rev.* **2012**, *112*, 5520.

(96) Gomes, W. P.; Cardon, F. *Prog. Surf. Sci.* **1982**, *12*, 155.

(97) Boonchun, A.; Umezawa, N.; Ohno, T.; Ouyang, S.; Ye, J. *J. Mater. Chem.* **2013**, *1*, 6664.

(98) Ohtani, B.; Iwai, K.; Nishimoto, S.; Sato, S. *J. Phys. Chem. B* **1997**, *5647*, 3349.

(99) Yang, J.; Wang, D.; Han, H.; Li, C. *Acc. Chem. Res.* **2013**, *46*, 1900.

(100) Zhou, P.; Li, Z.; Zou, Z. *Curr. Inorg. Chem.* **2012**, *2*, 184.

(101) Osterloh, F. E. *Chem. Soc. Rev.* **2013**, *42*, 2294.

(102) Kurihara, T.; Okutomi, H.; Miseki, Y.; Kato, H.; Kudo, A. *Chem. Lett.* **2006**, *35*, 274.

(103) Li, A.; Kato, H.; Kudo, A. *J. Phys. Chem. B* **2001**, *3*, 4285.

(104) Konta, R.; Kato, H.; Kobayashi, H.; Kudo, A. *Phys. Chem. Chem. Phys.* **2003**, *5*, 3061.

(105) Hwang, D. W.; Lee, J. S.; Li, W.; Oh, S. H. *J. Phys. Chem. B* **2012**, *7*, 4963.

(106) Brazhkin, V. V. *Physics-Uspekhi* **2006**, *49*, 719.

(107) Baricco, M.; Palumbo, M.; Baldissin, D.; Bosco, E.; Battezzati, L. *La Metall. Ital.* **2004**, 1.

(108) Jacobson, A. J.; Lewandowski, J. T.; Johnson, J. W. *Inorg. Chem.* **1985**, *24*, 3727.

(109) Gopalakrishnan, J.; Bhat, V. *Inorg. Chem.* **1987**, *26*, 4299.

(110) Schaak, R. E.; Mallouk, T. E. *Chem. Mater.* **2002**, *14*, 1455.

(111) Gopalakrishnan, J. *Chem. Mater.* **1995**, *7*, 1265.

(112) Alberti, G.; Conte, A.; Allulli, S. *J. Chromatog.* **1965**, *18*, 564.

(113) Gwon, H.; Kim, S.-W.; Park, Y.-U.; Hong, J.; Ceder, G.; Jeon, S.; Kang, K. *Inorg. Chem.* **2014**, *53*, 8083.

(114) Jacobson, A. J.; Lewandowski, J. T.; Johnson, J. W. *Mat. Res. Bull.* **1990**, *25*, 3.

(115) Jacobson, A. *J. Less-Common Met.* **1986**, *116*.

(116) Gopalakrishnan, J.; Bhat, V. *Mat. Res. Bull.* **1987**, *22*, 413.

(117) Stemmer, W.; Gruehn, R. *Z. Anorg. Allg. Chem.* **1993**, *619*, 409.

(118) Uma, S. *J. Mater. Chem.* **1993**, *3*, 709.

(119) Bhuvanesh, N. S. P.; Woodward, P. M. *J. Am. Chem. Soc.* **2002**, 14294.

(120) Cushing, B. L.; Wiley, J. B. *Mat. Res. Bull.* **1999**, *34*, 271.

(121) Moisseev, G.K. Surova, I.Y., T. *Russ. J. Inorg. Chem.* **2000**, *45*, 11.

(122) Jahnberg, L. Sundberg, M. *J. Solid State Chem.* **1992**, *100*, 212.

(123) Jahnberg, L. *Acta Chem. Scand. A* **1987**, *41*, 527.

(124) Liao, J.; Tsai, M. *Cryst. Growth Des.* **2002**, *2*, 22.

(125) Schmachtel, V. J.; Muller-Buschbaum, H. K. *Z. Anorg. Allg. Chem.* **1981**, *94*, 89.

(126) Roof, I. P.; Smith, M. D.; Cussen, E. J.; zur Loye, H.-C. *J. Solid State Chem.* **2009**, *182*, 295.

(127) Li, Y.; Hui, C.; Li, Y.; Wang, Y. *J. Alloy. Compnd.* **2011**, *509*, L203.

(128) Shi, Y.; Guo, Y.; Yu, S.; Arai, M.; Sato, A.; Belik, A. A.; Yamaura, K.; Takayama-Muromachi, E. *J. Am. Chem. Soc.* **2010**, *132*, 8474.

(129) Harre, N.; Mercurio, D.; Trolliard, G.; Frit, B. *Eur. J. Solid State Inorg. Chem.* **1998**, *35*, 77.

(130) Alablanche, S.; Thery, J.; Vivien, D. *Mat. Res. Bull.* **1989**, *24*, 475.

(131) Kitada, A.; Tsujimoto, Y.; Yamamoto, T.; Kobayashi, Y.; Narumi, Y.; Kindo, K.; Aczel, A. A.; Luke, G. M.; Uemura, Y. J.; Kiuchi, Y.; Ueda, Y.; Yoshimura, K.; Ajiro, Y.; Kageyama, H. *J. Solid State Chem.* **2012**, *185*, 10.

(132) Afanasiev, P. *J. Alloy. Compnd.* **2002**, *340*, 74.

(133) Mendoza-Mendoza, E.; Montemayor, S. M.; Escalante-García, J. I.; Fuentes, A. F. *J. Am. Ceram. Soc.* **2012**, *95*, 1276.

(134) Deloume, J.-P.; Marote, P.; Sigala, C.; Matei, C. *J. Solid State Chem.* **2003**, *174*, 1.

(135) Toda, K.; Watanabe, J.; Sato, M. *Solid State Ionics* **1996**, *90*, 15.

(136) Yamane, H.; Takahashi, H.; Kajiwara, T.; Shimada, M. *Acta Crystallogr. Sec. C* **1999**, *55*, 1978.

(137) Yamane, H.; Takahashi, H.; Kajiwara, T.; Shimada, M. *Acta Crystallogr. Sec. C* **2000**, *56*, 1177.

(138) Davis, M. J.; Smith, M. D.; zur Loye, H.-C. *J. Solid State Chem.* **2003**, *173*, 122.

(139) Sarapulova, a.; Mikhailova, D.; Senyshyn, A.; Ehrenberg, H. *J. Solid State Chem.* **2009**, *182*, 3262.

(140) Van der Lee, A.; Beaurain, M.; Armand, P. *Acta Crystallogr. Sec. C* **2008**, *64*, i1.

(141) Beaurain, M.; Armand, P.; Papet, P. *J. Cryst. Growth* **2005**, *275*, e279.

(142) Gatehouse, B. M.; Nesbit, M. C. *J. Solid State Chem.* **1981**, *6*, 1.

(143) Gatehouse, B. M.; Nesbit, M. C. *J. Solid State Chem.* **1980**, *33*, 153.

(144) Muller-Buschbaum, H.; Teichert, A. *J. Less-Common Met.* **1990**, *170*, 315.

(145) Ostorero, J.; Nanot, M.; Queyroux, F.; Gilles, J. C.; Makram, H. *J. Cryst. Growth* **1983**, *65*, 576.

(146) Sun, B. N.; Boutellier, R.; Sciau, P.; Burkhardt, E.; Rodriguez, V.; Schmid, H. *J. Cryst. Growth* **1991**, *112*, 71.

(147) Tellier, J.; Boullay, P.; Manier, M.; Mercurio, D. *J. Solid State Chem.* **2004**, *177*, 1829.

(148) Giaquinta, D. M.; Papaefthymiou, G. C.; Davis, W. M.; zur Loye, H. C. *J. Solid State Chem.* **1992**, *99*, 120.

(149) Giaquinta, D. M.; zur Loye, H. C. *J. Alloy. Compnd.* **1992**, *184*, 151.

(150) Huang, J.; Sleight, A. W. *J. Solid State Chem.* **1992**, *100*, 170.

(151) Mercurio, D.; Trolliard, G.; Hansen, T.; Mercurio, J. . *Int. J. Inorg. Mater.* **2000**, *2*, 397.

Table 1. Various commonly used fluxes and their melting temperatures are listed with the metal-oxides that have been successfully synthesized utilizing these molten fluxes.

Flux	Melting Point (°C)	Materials Synthesized with Flux
NaCl	801	$Na_2Ca_2Nb_4O_{13}$[23], $PbTiO_3$[13], $SrTiO_3$[29]
KCl	771	$K_2BiNb_5O_{15}$[127], Ca_3LiOsO_6[128], $SrTiO_3$[29], $Sr_3Ti_2O_7$[41]
NaCl/KCl	657	Sr_2FeReO_6, Sr_2CrReO_6, Ba_2FeReO_6[17]
RbCl	720	$RbLaNb_2O_7$[24]
$BaCl_2$	962	$Ba_2La_4Ti_5O_{18}$[129], $BaMg_6Ti_6O_{19}$[130]
CuCl	426	$CuNb_3O_8$[38], $Cu_2Nb_8O_{21}$[15], $Cu_5Ta_{11}O_{30}$, $Cu_3Ta_7O_{19}$[16]
$CuCl_2$	498	$(CuCl)Ca_2NaNb_4O_{13}$[131], $(CuCl)Ca_2B_3O_{10}$, $(CuCl)LaB_2O_7$ (B = Nb, Ta)[30]
$SnCl_2$	247	$SnNb_2O_6$[20]
$PbCl_2$	501	$Pb_{1.5}Ta_7O_{19}$,[117] $PbTa_4O_{11}$, $Pb_3Ta_4O_{13}$[27,117]
Na_2SO_4	884	$Na_2Ca_2Nb_4O_{13}$[23], $AgNbO_3$[12]
$KHSO_4$	214	$(CuCl)Ca_2B_3O_{10}$, $(CuCl)LaB_2O_7$ (B = Nb, Ta)[30]
Na_2SO_4/K_2SO_4	834	$La_2Ti_2O_7$[25], $Na_2Ta_4O_{11}$[19], La-$NaTaO_3$[21], $Bi_5Ti_3FeO_{15}$, $LaBi_4Ti_3FeO_{15}$[42]
$NaNO_3$	310	$Ce_{0.75}Zr_{0.25}O_2$[132], $LaAlO_3$[133]
KNO_3	337	$(CuCl)Ca_2B_3O_{10}$, $(CuCl)LaB_2O_7$ (B = Nb, Ta)[30], $LaAlO_3$[133]
$NaNO_3/KNO_3$	223	AWO_4 (A = Mg, Ba, Ca, Ni, Cu, Zn)[134]
$AgNO_3$	212	$AgLaNb_2O_7$, $AgA_2Nb_3O_{10}$ (A = Ca, Sr),[26] $Ag_2La_2Ti_3O_{10}$[26,135]
Na_2CO_3	851	$Ca_2Na_3TaO_6$[136], $Ca_3Na_2Ta_2O_9$[137]
K_2CO_3	891	Ca_3CuRhO_6, Ca_3FeRhO_6[138]
$SrCO_3$		$SrTiO_3$[61]
LiOH	477	$La_3Li_5Ta_2O_{12}$, $Li_5Nd_3Ta_2O_{12}$, $Li_5Pr_3Ta_2O_{12}$[126]
NaOH	320	$Al_2Ba_4Ti_{10}O_{27}$[125], $LnFeO_3$ (Ln = La, Pr, Nd)[22]
KOH	404	KLa_2NbO_6[31]
KOH/NaOH	170	$KLaNaNbO_5$, $K_2Na_2Sm_4Ta_2O_{13}$[57]
KOH/LiOH	225	La_2LiOsO_6, $LiNd_2OsO_6$[56]
Li_2MoO_4	705	$CrLiMo_2O_8$, $CrLi_3Mo_3O_{12}$[139]
$Li_2Mo_3O_{10}$	560	$GaLiMo_2O_8$, $GaLi_3Mo_3O_{12}$[140,141]
MoO_3	795	$KTaTi_3O_9$[142], $KTa_5Ti_2O_{17}$[143]
PbO	888	$Al_{10}MnPb_3O_{20}$[144], $Ca_2Nd_4Ti_6O_{20}$[145], $CoPb_2WO_6$[146]
Bi_2O_3	817	$Bi_4CaTi_4O_{15}$[147], $Bi_2Fe_2Ga_2O_9$[148],

	$Bi_2Fe_2Mn_2O_{10}$[149], $BiMg_2VO_6$[150], $Bi_7NbTi_4O_{21}$[151]

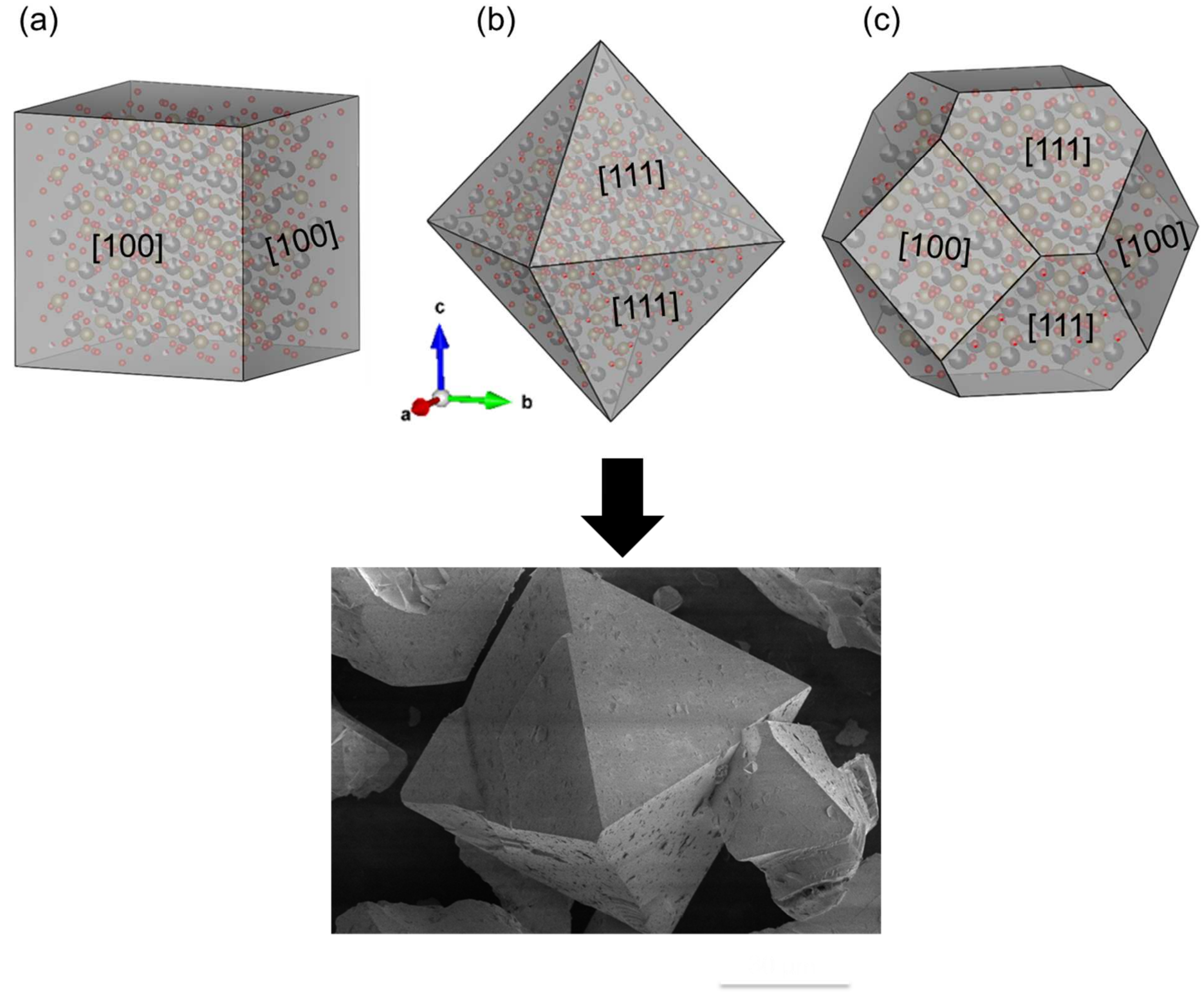

Figure 1. Cubic crystal structures ($Fd\bar{3}m$) can exhibit (a) cube, (b) octahedron, and (c) cuboctahedron particle morphologies with exposure of the [100], [111], and [100]/[111] faces, respectively as shown by the SEM image for $Pb_3Ta_4O_{13}$.

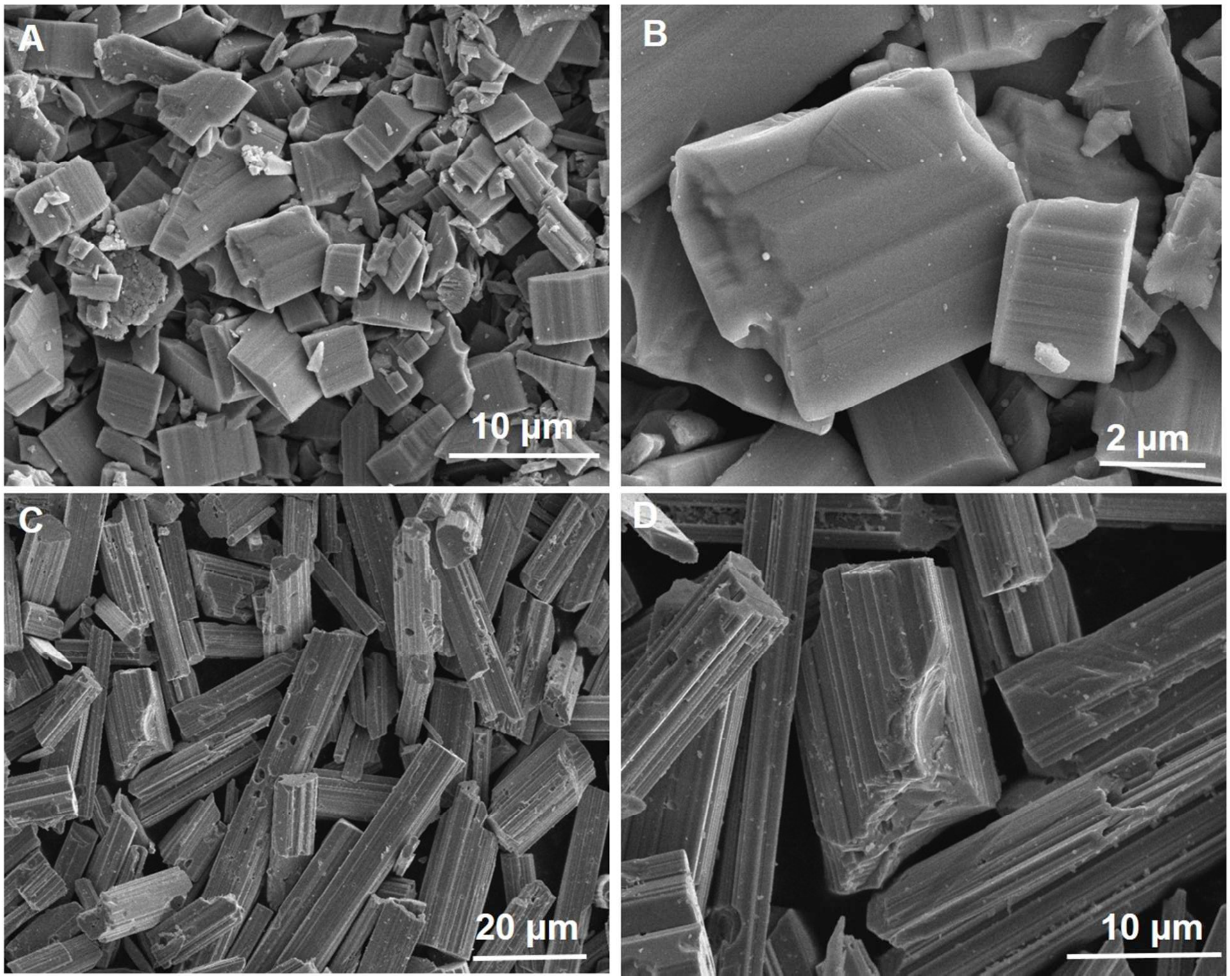

Figure 2. SEM images of $CuNb_3O_8$ and $Cu_2Nb_8O_{21}$ after flux synthesis at 750 °C for 15 min (a-b) and at 550 °C for 24 h (c-d), respectively. The products from both reactions were quenched in air immediately after heating.

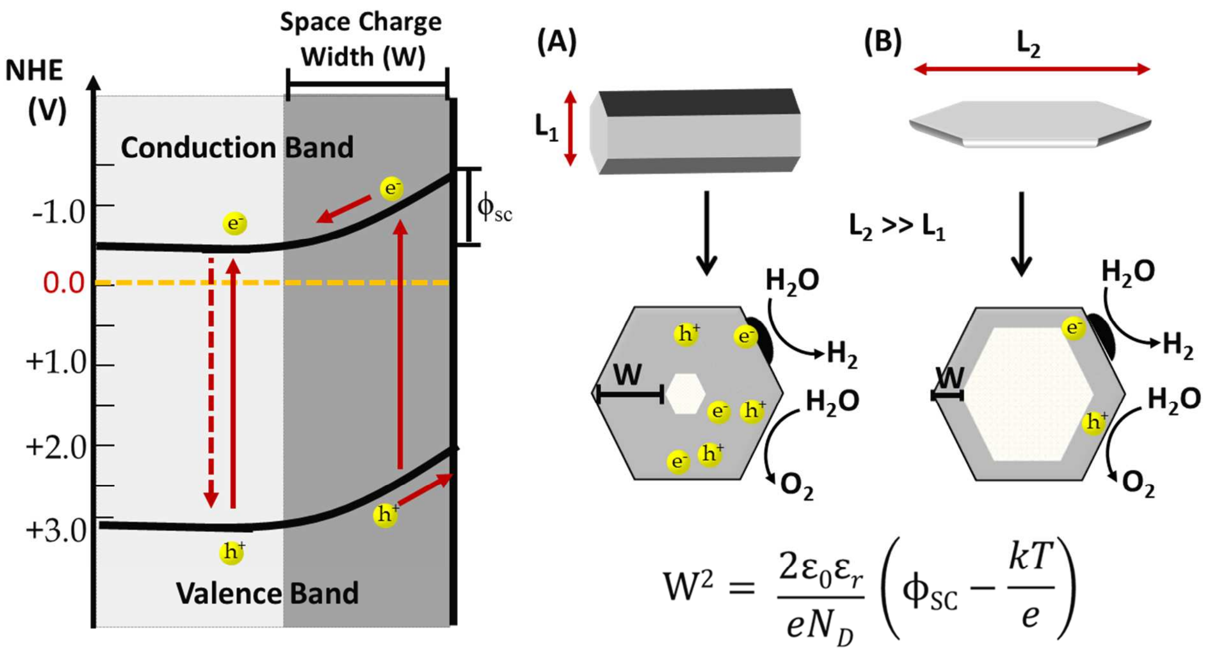

$$W^2 = \frac{2\varepsilon_0\varepsilon_r}{eN_D}\left(\phi_{SC} - \frac{kT}{e}\right)$$

Figure 3. On left, formation of a space charge layer width (W) that drives the separation of excited electron-hole pairs; On right, comparison of the space charge width within rod-shaped (A) versus platelet-shaped particles (B). W is shown to cover a much larger percentage of particle volume in the former. Variable definitions given in text.

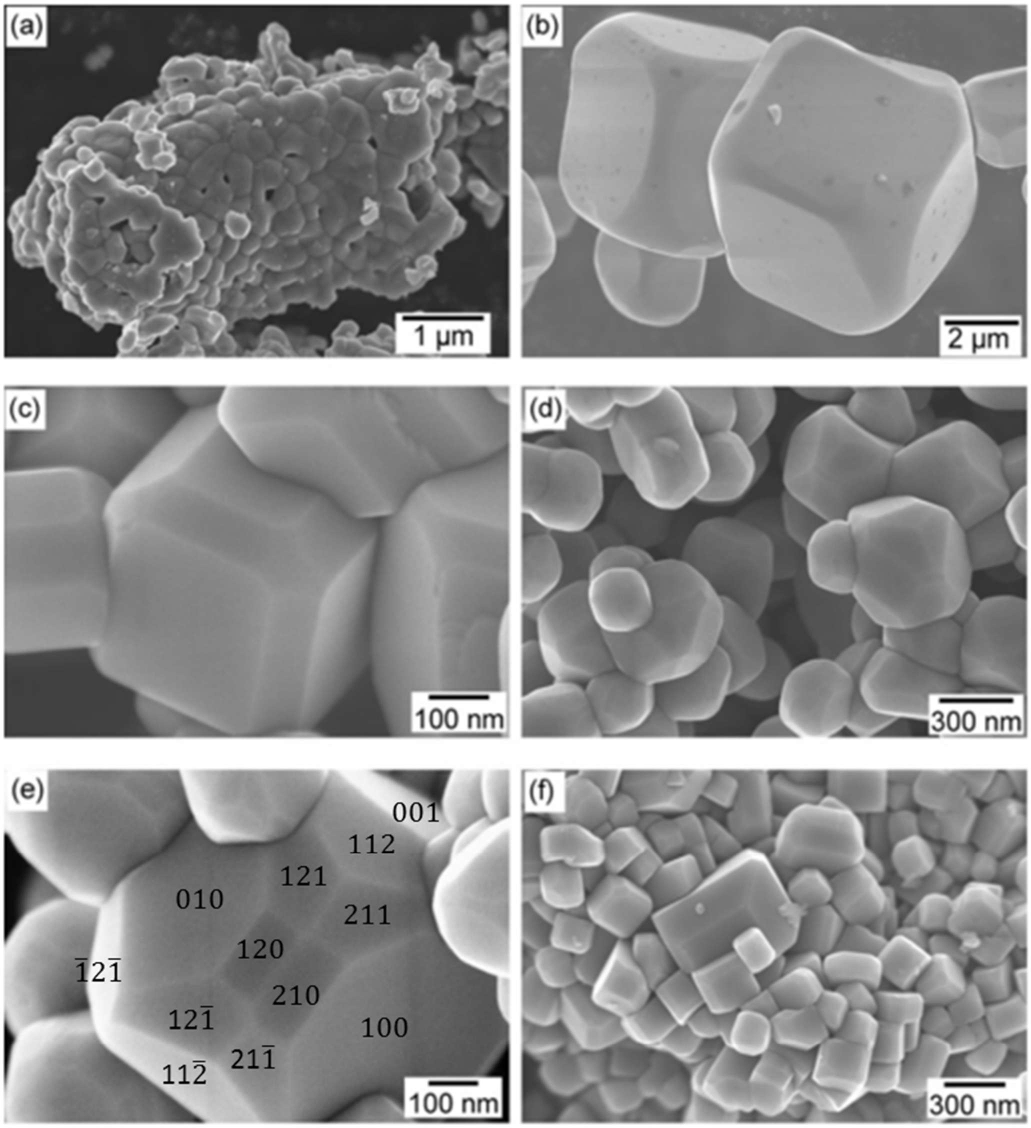

Figure 4. SEM images of $SrTiO_3$ prepared (a) by conventional solid-state methods and by flux methods using a (b) LiCl, (c) NaCl, (d and e) KCl, and (f) $SrCl_2$ flux. The exposed crystal facets are labeled with their appropriate Miller indices for KCl (e). Reprinted (adapted) with permission from the Royal Society of Chemistry.[29]

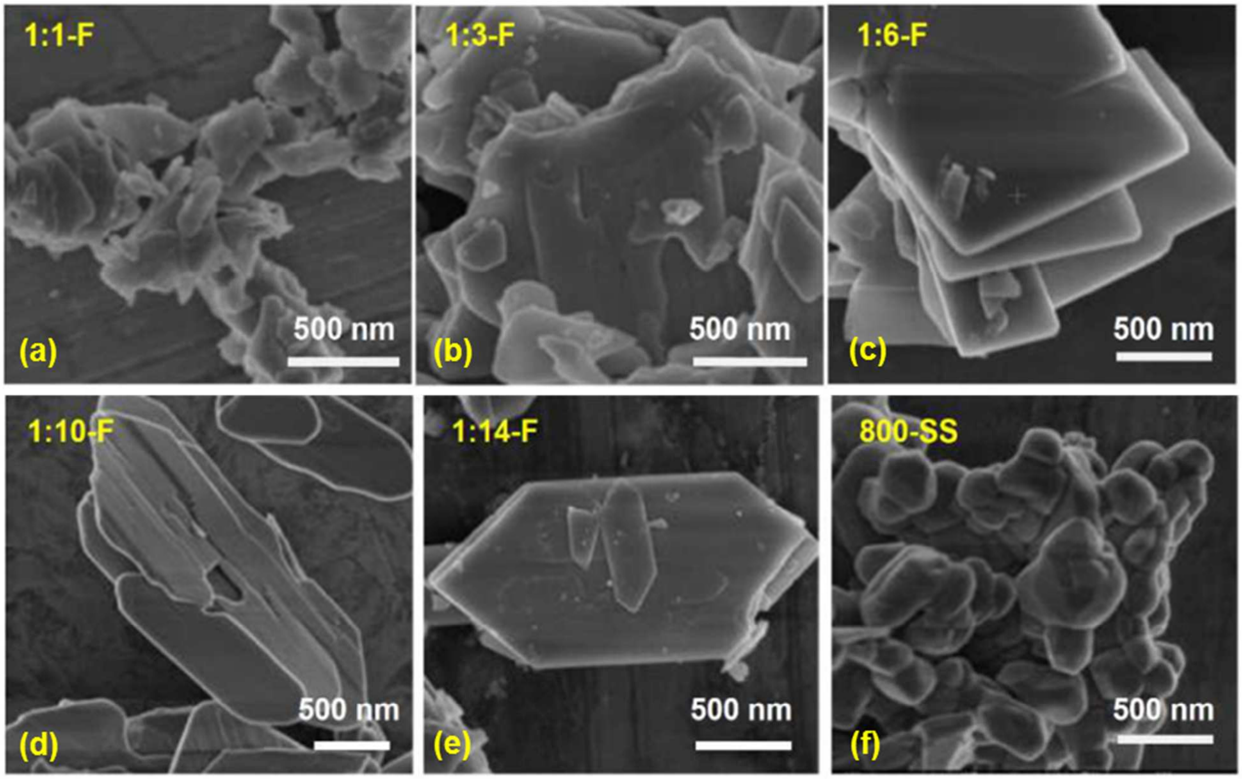

Figure 5. SEM images of $SnNb_2O_6$ prepared by flux methods using (a) 1:1, (b) 1:3, (c) 1:6, (d) 1:10, and (e) 1:14 reactant-to-flux molar ratios and by conventional (f) solid-state methods at 800 °C. Reprinted (adapted) with permission from the Royal Society of Chemistry.[20]

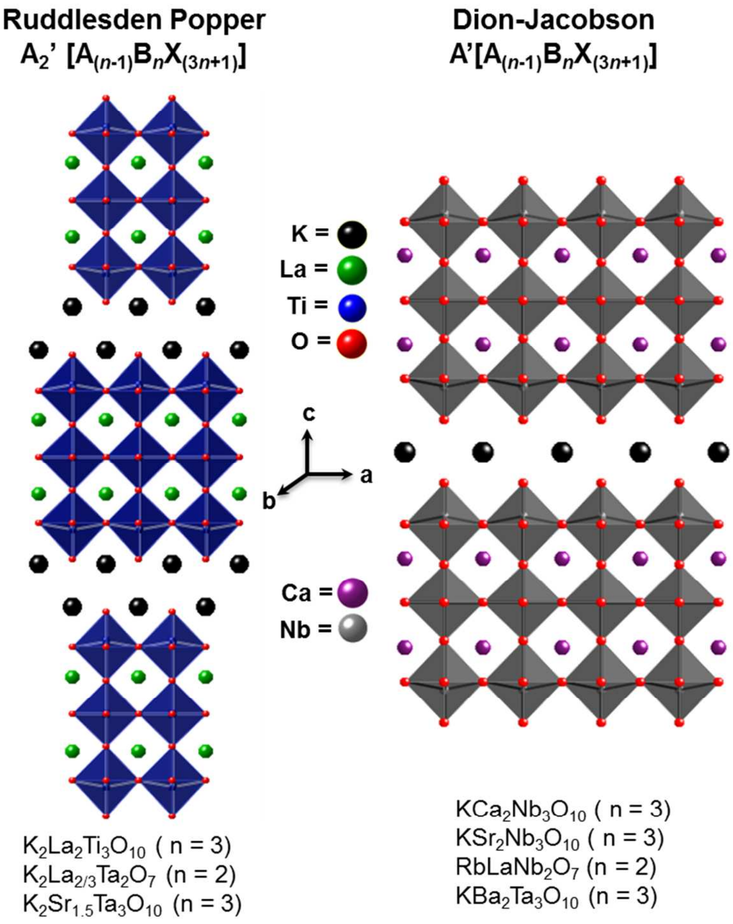

Figure 6. Structures for the Dion-Jacobson phase $K_2La_2Ti_3O_{10}$ and the Ruddlesden Popper phase $KCa_2Nb_3O_{10}$ are shown with other examples of these layered perovskite structures listed below.

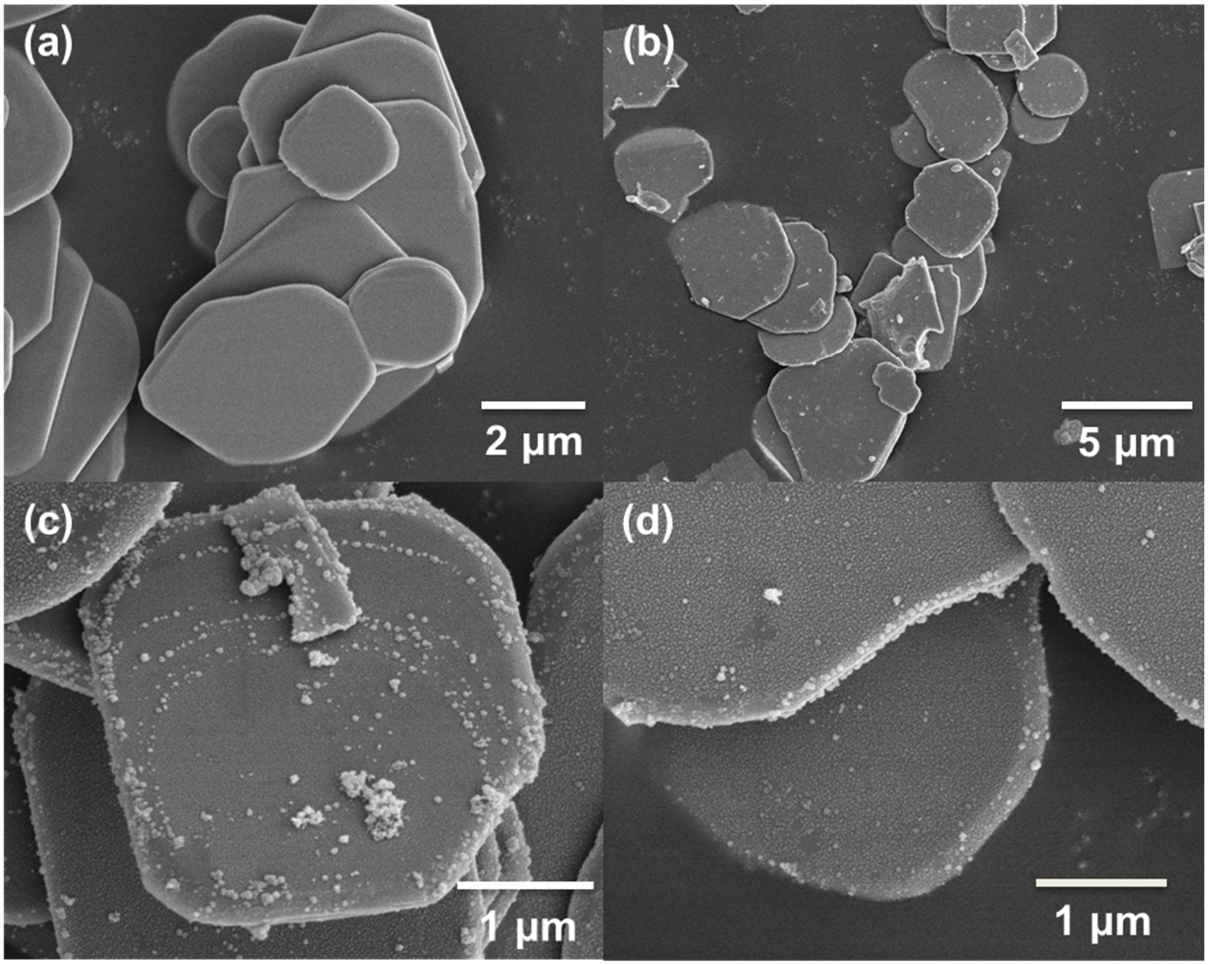

Figure 7. FESEM images of the flux prepared $RbLaNb_2O_7$ using a 10:1 RbCl flux (a), after the silver-exchange reaction to yield $AgLaNb_2O_7$ (b), and $RbLaNb_2O_7$ after the photodeposition of 5% wt. Pt(s) (c, d).[24]

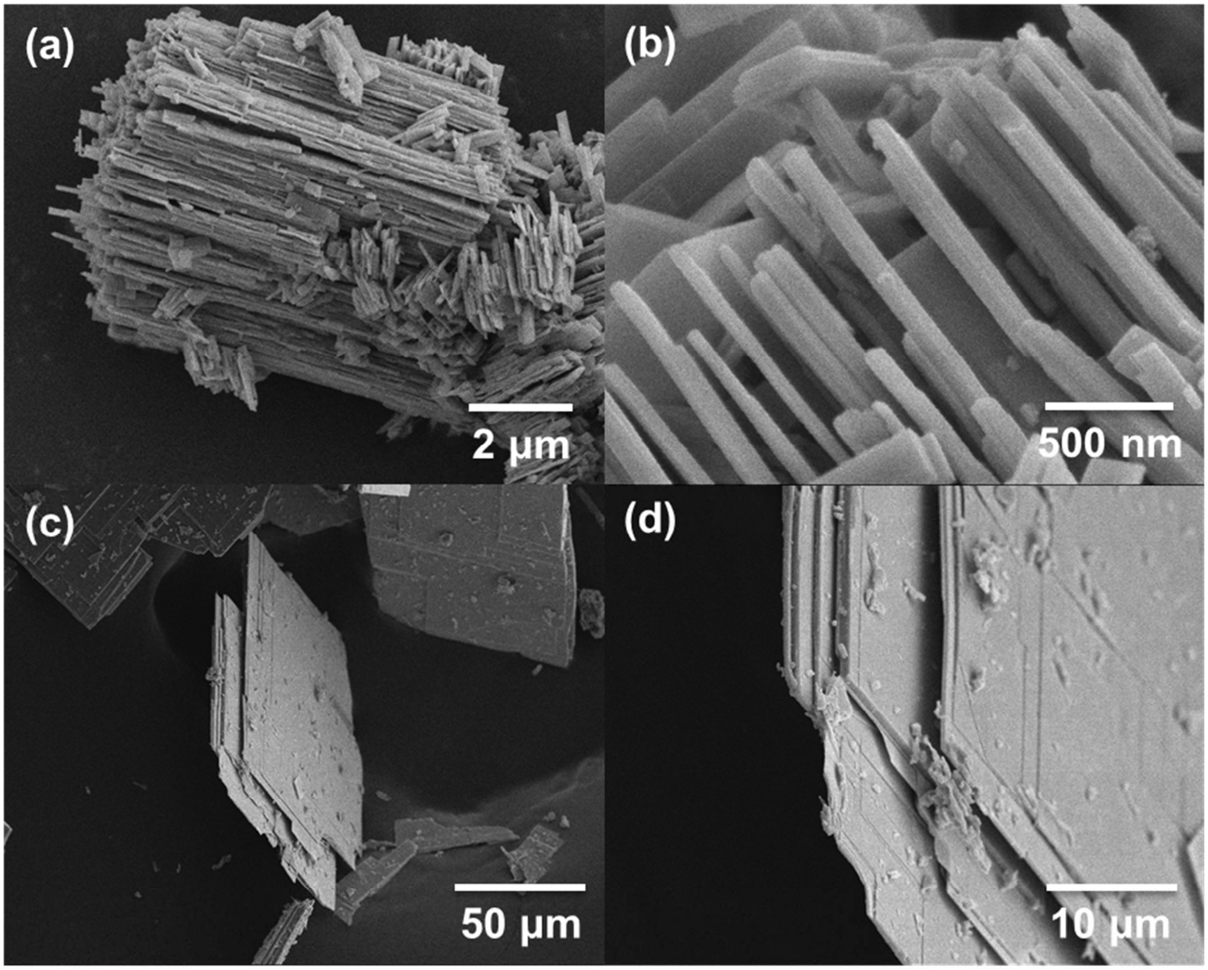

Figure 8. SEM Images of $Na_2Ca_2Nb_4O_{13}$ particles prepared using a 5:1 NaCl (a, b) and a 5:1 Na_2SO_4 flux (c, d) yielding rod and platelet morphologies. [23]

Figure 9. A schematic of the flux-mediated crystal growth of (A) rod-shaped particles of $PbTa_4O_{11}$ and (B) platelet-shaped particles of $RbLaNb_2O_7$ photocatalysts. Resulting differences in the match of their space charge widths to their particle sizes and shapes are illustrated, with a larger coverage shown for $PbTa_4O_{11}$.

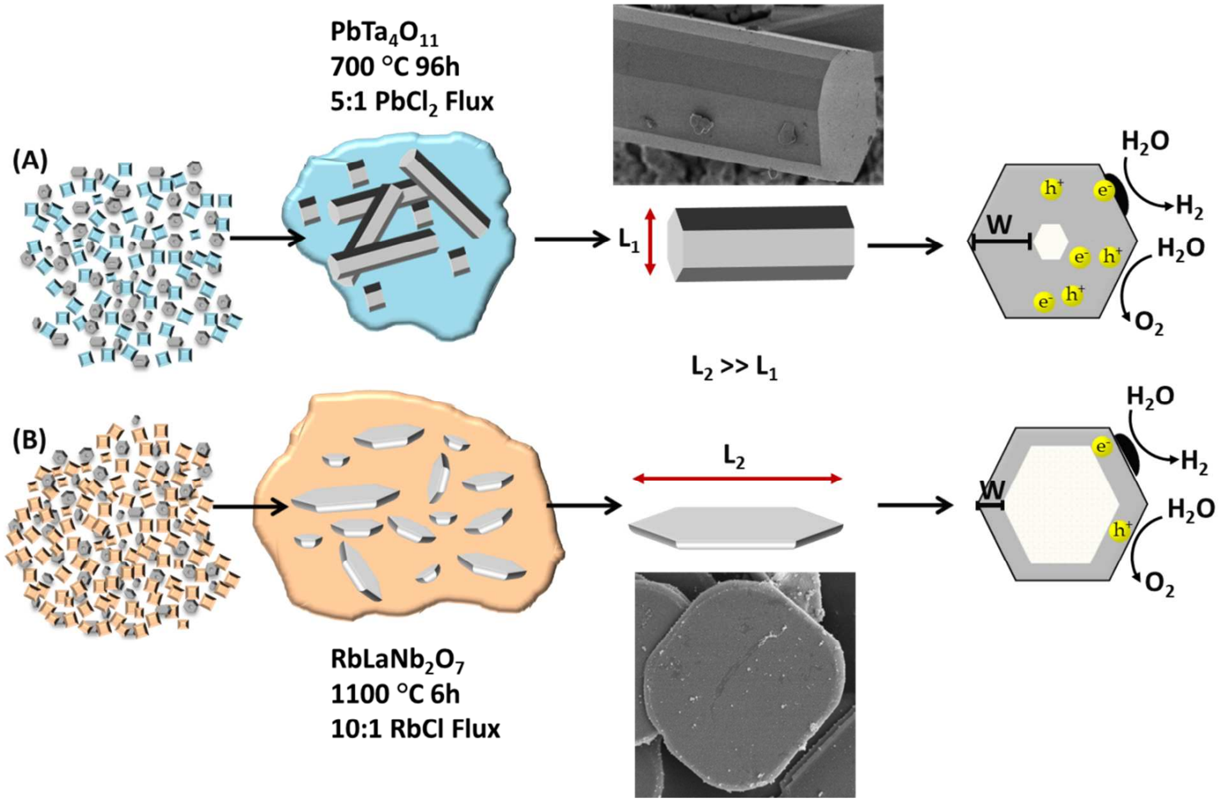

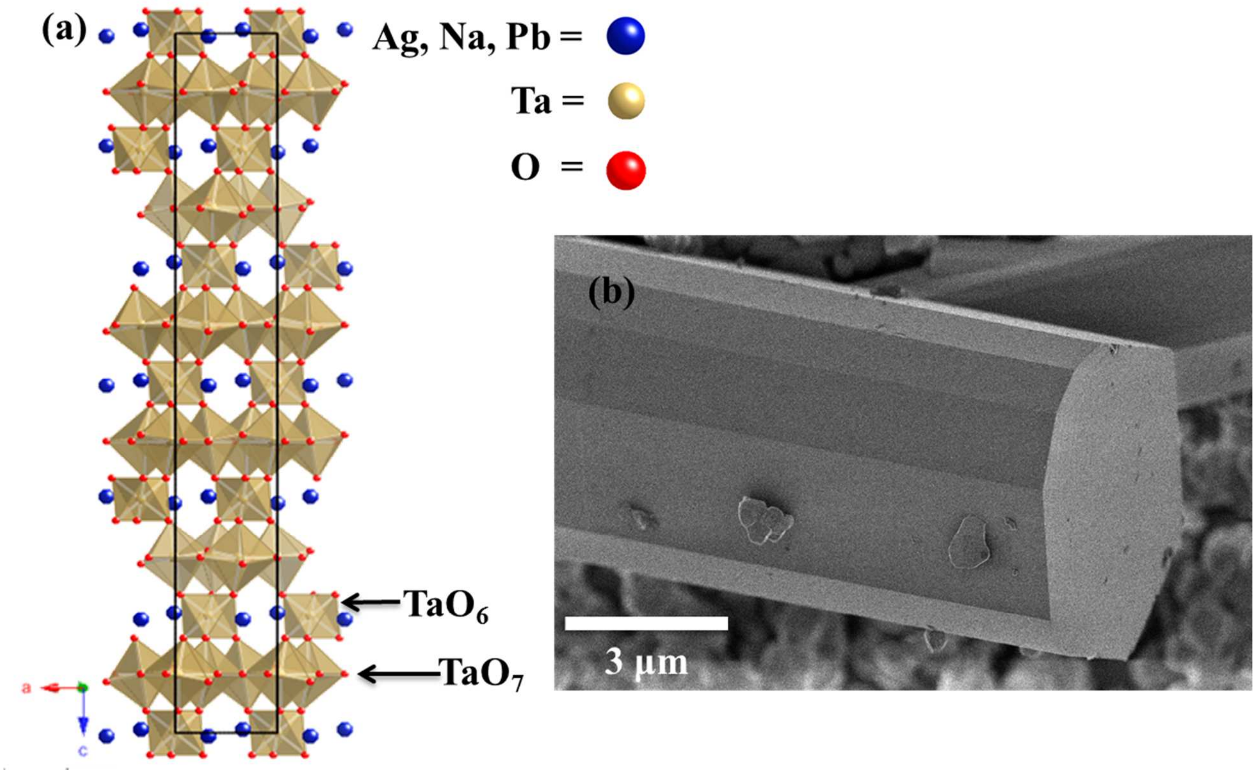

Figure 10. Polyhedral view of the (a) overall unit cell of $A^{m+}_{(n+1)/m}Ta_4O_{11}$ (A = Na, Ag, Pb; $n = 1$; $m = 1, 2$) consisting of TaO_7 pentagonal bipyramid layers alternating with isolated TaO_6 octahedra surrounded by Na(I), Ag(I), or Pb(II) cations along the *c* axis. An SEM image of the resulting (b) rod-shaped particle of $PbTa_4O_{11}$ is shown.[27]

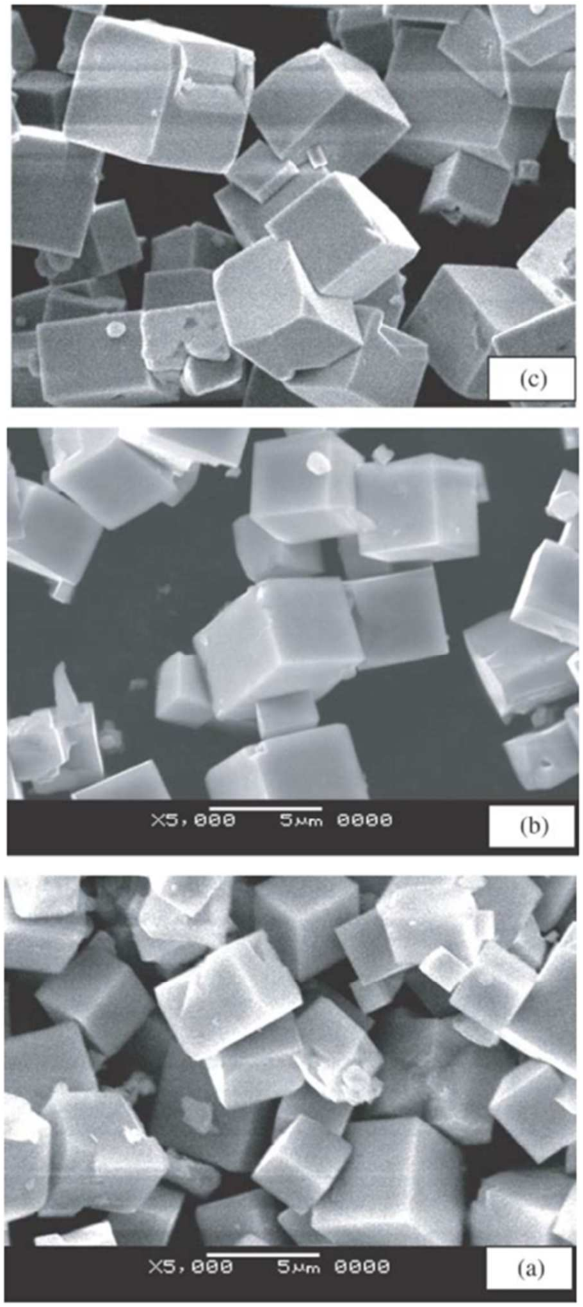

Figure 11. SEM images of (a) $LaFeO_3$, (b) $PrFeO_3$, and (c) $NdFeO_3$ prepared using a NaOH flux. Reprinted (adapted) with permission from Elsevier.[22]